Chapter 22
High-Speed Atomic Force Microscopy

Takayuki Uchihashi, Noriyuki Kodera and Toshio Ando

Abstract High-speed atomic force microscopy (HS-AFM) has now been established that can capture protein molecules in action at submolecular spatial and sub-100 ms temporal resolution, without disturbing their biological function. In fact, various application studies on proteins have demonstrated this capability and brought important discoveries that cannot be achieved by other approaches. Moreover, recent progress of HS-AFM techniques has been extending its use to the observation of dynamic events occurring in larger samples including live cells and isolated intracellular organelles. This review mostly focuses on various techniques that have led to the achievement of these capabilities of HS-AFM, together with brief descriptions of typical application studies of proteins.

22.1 Introduction

AFM is a leading-edge driving force for the creation of new techniques, new research areas and new nanotech industries. Since the birth of AFM, its technology has been continuously advanced and extended in various directions. For example, efforts have been carried out to pursue the ultimate high spatial resolution and force sensitivity

T. Uchihashi · T. Ando (✉)
Department of Physics, Institute of Science and Engineering, Kanazawa University, Kakuma-machi, Kanazawa 920-1192, Japan
e-mail: tando@staff.kanazawa-u.ac.jp

T. Uchihashi · N. Kodera · T. Ando
Bio-AFM Frontier Research Center, Institute of Science and Engineering, Kanazawa University, Kakuma-machi, Kanazawa 920-1192, Japan
e-mail: uchihast@staff.kanazawa-u.ac.jp

T. Uchihashi · T. Ando
CREST, Japan Science and Technology Agency, 4-1-8 Honcho, Kawaguchi 332-0012, Japan

N. Kodera
PRESTO, Japan Science and Technology Agency, 4-1-8 Honcho, Kawaguchi 332-0012, Japan
e-mail: nkodera@staff.kanazawa-u.ac.jp

S. Morita et al. (eds.), *Noncontact Atomic Force Microscopy*, NanoScience and Technology, DOI 10.1007/978-3-319-15588-3_22

of AFM. Consequently, it has now become possible to visualize even sub-atomic structures [1], distinguish the species of atoms on a solid surface [2] and resolve single electron spins [3]. These ultimate capabilities are based on the high quality mechanical resonance of cantilevers or quartz tuning forks [4] in vacuum. In non-vacuum usage of AFM, efforts have been directed to the acquisition of local material property maps of objects, in addition to their surface topography. The local material properties that have been acquired are elastic and adhesive properties [5, 6], magnetic and electric properties [7, 8], heat conductivity [9] and others. Similarly, various AFM systems have been developed that are combined with fluorescence microscopy, Raman spectroscopy, infrared spectroscopy, acoustic techniques [10, 11] and microwave techniques [12]. Some of the developed instruments are now of practical use for the inspection of industrial products. Moreover, AFM has been adapted to develop techniques for surface nano-processing, such as nano-printing [13] and nano-lithography [14]. Thus, beyond the initial aim and perspective, the AFM technology has been quickly extended into various directions and used in diverse areas.

In stark contrast to the remarkable rapid advances mentioned above, the slow scan and hence the low imaging rate of AFM has remained unimproved until very recently. Even now in 2014 when we are writing this chapter, more than 99 % of all AFM instruments that are in use worldwide remain slow. Maybe, this delay of progress would arise from the fact that the use of AFM has mainly been focused on the acquisition of high-resolution images of objects and force spectroscopy data. As a matter of course, high imaging rates cannot be anticipated in-vacuum NC-AFM because the high quality mechanical resonance of the probes is incompatible with fast response to an exerted force, and because there may not be many interesting dynamic phenomena to visualize in vacuum, at the nanometer scale. However, in gas and liquid environments, there are many interesting dynamic phenomena to study at the nanometer scale. In particular, most of biomolecular phenomena occur dynamically in aqueous solutions. Therefore, it may be understandable that one of the biophysicists writing this chapter (TA) embarked on the development of high-speed AFM (HS-AFM) in 1993. His group continued to work towards its materialization [15, 16] and finally demonstrated the innovative power of HS-AFM by capturing dynamics images of protein molecules in action: for example, bacteriorhodopsin in response to light [17], myosin V walking on actin filaments [18], rotor-less F_1-ATPase undergoing rotary propagation of conformational changes [19] and celluloses moving on cellulose fibers while hydrolyzing the fibers [20]. However, note that the initial attempt to increase the imaging rate of AFM was made by Quate and colleagues in 1991 to acquire wide-area images of semiconductor wafers [21] and produce nano-patterns on wide-area surfaces in a relatively short time [22] (a historical view of HS-AFM development is described elsewhere [23]). In addition to biomolecular phenomena for which the merit of HS-AFM has plainly been put forth, there are an array of dynamic phenomena occurring in liquids which are worth to be visualized at high rates: for example, corrosion reactions of metallic materials, electrochemical reactions represented by those in batteries, catalytic reactions, cleaning by detergents and dissolution of photoresists. Except for the dissolution of photoresist [24], these

dynamic phenomena have never been visualized at the nanometer scale and enough time resolution. As aimed by the Quate group, the high-speed performance is also important even in the acquisition of still images of topography and material property maps of surfaces because it permits in-depth and wide-area analysis of the surfaces within realistic time periods. These significant merits to be brought by high-speed imaging have recently been recognized in the AFM community. As a result, a number of researchers in various areas, including mechanical engineering and control engineering, have now been participating in developing techniques that may serve to improve the imaging rate of AFM. However, most of these studies focus on only one of various techniques involved in AFM. Therefore, it is often difficult to judge the actual usefulness of developed techniques.

Thus far, HS-AFM has been established only in in-liquid AFM and used most exclusively for biological studies. However, there must be a definite demand for increasing the speed performance of any type of AFM instruments and more generally any type of scanning probe microscopy (SPM) instruments. This chapter is dedicated mostly to describing HS-AFM techniques not only of the authors' group but also of others, which, we hope, will be good references for future developers of HS-SPM instruments. Before technical details, theoretical considerations are given to provide a quantitative relationship that determines the maximum possible imaging rate as a function of various parameters. After technical descriptions, representative HS-AFM imaging studies are presented. Finally, this chapter is closed with future prospects of HS-AFM.

22.2 Theoretical Considerations

The highest possible imaging rate of AFM, $R_{\max}$ frames/s (fps), is a function of various parameters and depends on the imaging mode. Here we quantitatively describe $R_{\max}$ in tapping mode AFM that employs a raster scan of the sample stage in the horizontal plane. For simplicity, the sample surface is assumed to have a sinusoidal shape with a periodicity λ and the maximum height h_0 in the XZ plane; height h varies as $h(x) = (h_0/2) \times [\sin(2\pi x/\lambda) + 1]$. When the sample stage is moved in the X-direction at velocity V_s and no feedback scan of the Z-scanner is performed, the sample height under the cantilever tip changes with time as $h(t) = (h_0/2) \times [\sin(2\pi ft) + 1]$, as shown with the solid line in Fig. 22.1a (here, the frequency f is given by $f = V_s/\lambda$). By feedback operation, the Z-scanner is moved at feedback frequency f in the direction opposite to the sample height. Because of the time delay τ_0 in the closed-loop feedback control, the Z-scanner is moved so that the sample-stage height $Z(t)$ changes as $Z(t) = -(h_0/2) \times [\sin(2\pi ft - \theta_0) + 1]$, where $\theta_0 = 2\pi f\tau_0$ is a phase delay in the sample surface tracing by feedback scan (the broken line in Fig. 22.1a). Therefore, the sample surface height $H(t)$, when viewed from the cantilever, cannot look perfectly flat but changes as

$$H(t) = h(t) + Z(t) = h_0 \sin(\theta_0/2) \times \cos(2\pi ft - \theta_0/2), \tag{22.1}$$

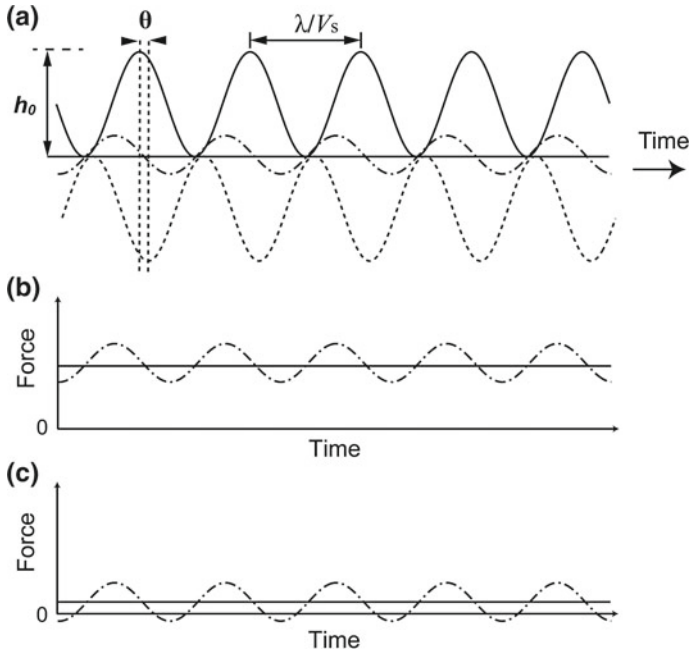

Fig. 22.1 Effect of feedback delay on the tip force exerted onto the sample. **a** Movement of Z-scanner (*broken line*) tracing the sinusoidally shaped sample surface (*solid line*; spatial periodicity, λ; temporal periodicity, λ/V_s; amplitude, $h_0/2$) that is being scanned in the X-direction at velocity V_s. Because of the delay of the Z-scanner movement, tracing error (*dashed line*) is produced. **b** Tip force (*dashed line*) exerted onto the sample when the set point force (*solid line*) corresponding to the set point amplitude is relatively large. **c** Tip force (*dashed*) exerted onto the sample when the set point force (*solid*) is set at a small value. The negative force cannot be exerted but becomes zero due to complete loss of tip-sample interaction when attractive tip-sample interaction is negligible

as shown with the dashed line in Fig. 22.1a. $H(t)$ represents the feedback error. Because of this error, the tapping force exerting from the oscillating cantilever tip to the sample cannot be maintained constant at the set point force (solid line in Fig. 22.1b) but varies; larger forces are exerted in the uphill regions of the sample, whereas weaker forces are exerted in the downhill regions, as shown with the dashed line in Fig. 22.1b. When the excessive force exerting on the sample is too excessive, we have to decrease the set point force (solid lines in Fig. 22.1c). This can be done by setting the cantilever set point amplitude A_s closer to the free oscillation amplitude A_0 (in other words, the dimensionless set point r defined as $r \equiv A_s/A_0$ is set closer to 1). However, this new setting results in a situation where the tip force to act on the sample in steep downhill regions becomes negative or zero (dashed line in Fig. 22.1c). Even under this situation, the tip can be kept in contact with the sample, if a sufficient attractive interaction (i.e., negative force) occurs between the tip and the sample. However, in the case of biological samples in physiological buffer solutions, the attractive tip-sample interaction is negligibly small and therefore the tip easily

loses contact. Once the contact is lost, it takes time for the tip to land on the sample surface again (like parachuting), because the error signal is saturated at a small value, $A_0(1-r)$, irrespective of how far the tip is apart from the sample surface at its bottom swing. Thus, it is now clear that the sample fragility significantly limits the largest allowable phase delay $\theta_{\max}$ and hence the maximum possible scan speed $V_s^{\max}$. In other words, low-invasive imaging is hard to be made compatible with high-speed imaging.

In general, the bandwidth f_B of closed feedback systems is defined by the feedback frequency at which $\pi/4$ radian (or 45°) phase delay occurs in the feedback control, i.e., $f_B = 1/(8\tau_0)$. Therefore, the $V_s^{\max}$ can be given by $V_s^{\max} = \lambda f_B \times \theta_{\max}/(\pi/4)$. Under the imaging conditions of the scan range in the X-direction W and the number of scan lines N, an image acquisition time T is given by $T = 2WN/V_s$. Thus, the maximum possible imaging rate $R_{\max}$ is given by

$$R_{\max} = 2\lambda f_B \theta_{\max}/(\pi WN). \tag{22.2}$$

Next, we quantitatively estimate how significantly $\theta_{\max}$ is limited by the tip-parachuting effect, assuming that attractive tip-sample interactions are negligibly small. The condition under which no complete loss of tip-sample contact occurs is given by $H(t) + A_0(1-r) > 0$ at any time, which results in

$$A_0(1-r) - h_0 \sin(\theta_0/2) > 0. \tag{22.3}$$

Under the conditions of $A_0 = h_0/5$ and $r = 0.9$ that are often employed for low-invasive imaging of protein molecules in solutions [25], equation (22.3) gives $\theta_0 < 0.013 \times \pi$ radian (i.e., $\theta_{\max} = 0.013 \times \pi$). This small value of $\theta_{\max}$ limits the highest possible feedback frequency to $\sim f_B/20$. As such, $R_{\max}$ is significantly restrained by the tip-parachuting problem. Thus, it is evident that HS-AFM applicable to fragile biological samples would not be materialized without finding a new feedback control technique that can eliminate the parachuting problem. As will be described later, such a technique has already been devised [26].

To increase the feedback bandwidth f_B, the time delay τ_0 of the closed-loop feedback control system has to be significantly reduced. To do so, the time delay of every device contained in the feedback loop has to be dramatically reduced. In the following sections, details of technical developments for this accomplishment are described.

22.3 Cantilever and Tip

The cantilever is a component most critical in accomplishing a high-speed imaging capability of AFM. Its mechanical properties significantly affect the bandwidth of feedback control. First of all, in the tapping mode, the probe tip should tap the sample surface at least once for each pixel of the image. Therefore, the cantilever's

first resonant frequency f_c should be high. The transient response of cantilever's oscillation amplitude to tip-sample contact should also be fast. The response rate is given by $\pi f_c/Q_c$, where Q_c is a quality factor. It may not be difficult to increase f_c by making the cantilever stiffer. However, a stiff cantilever exerts a large tapping force onto the sample and hence easily damages fragile samples. The first resonant frequency f_c and the spring constant k_c of a rectangular cantilever with thickness d, width w and length L are expressed as follows:

$$f_c = 0.56\frac{d}{L^2}\sqrt{\frac{E}{12\rho}} \tag{22.4}$$

and

$$k_c = \frac{wd^3}{4L^3}E, \tag{22.5}$$

where E and ρ are the Young's modulus and density of the material used, respectively. As is clear from these equations, the two demands, high f_c and small k_c, inherently conflicts and can only be achieved by miniaturization of the cantilever.

Small cantilevers have advantages in achieving not only high-speed imaging but also high sensitivity of force detection. The force detection sensitivity of AFM is generally limited by the extent of cantilever's thermal motion that is governed by the spring constant and the temperature; its average amplitude is given by $\sqrt{k_B T / k_c}$, where k_B is Boltzmann's constant and T is the temperature in Kelvin of measurement. The cantilever's thermal fluctuations in deflection are distributed over a frequency range from zero to slightly higher than f_c. Therefore, the thermal noise spectrum density becomes smaller for a cantilever with a higher f_c. In tapping-mode AFM, the frequency region used for imaging is approximately the imaging (or feedback) bandwidth centered at f_c. Thus, under a given k_c, the measurement of cantilever oscillation amplitude is less affected by thermal noise when cantilevers with higher f_c are used. Moreover, shorter cantilevers provide higher sensitivity in the optical beam deflection (OBD) detection of cantilever deflection, because the OBD method detects an angle change of a cantilever which follows $\Delta\varphi = 3\Delta z/(2L)$, where Δz and $\Delta\varphi$ are the displacement and angle change of the free end of the cantilever, respectively [27].

In the fabrication of small cantilevers with small k_c, silicon nitride (Si_3N_4) is usually used as a material. Its Young's modulus and density are $E = 2.9 \times 10^{11}$ N/m^2 and $\rho = 3200$ kg/m^3, respectively. For instance, when $f_c = 3$ MHz and $k_c = 0.2$ N/m are demanded for cantilevers, their feasible dimensions are $L \sim 7\,\mu$m, $d \sim 0.1\,\mu$m and $w \sim 1\,\mu$m, approximately one-tenth of those of conventional cantilevers. Several groups have attempted to fabricate small cantilevers [28–33]. Cantilevers satisfying both high f_c and small k_c have been successfully developed by Olympus, using low-pressure chemical vapor deposition (LP-CVD) that can precisely control the thickness of a Si_3N_4 film [31]. The custom-made small cantilevers that we are currently using have dimensions of $L = 6$–$7\,\mu$m, $w = 2\,\mu$m and $d = 90$ nm,

which provide $f_c = \sim 3.5$ MHz in air, $f_c = \sim 1.2$ MHz in water, $k_c = \sim 0.2$ N/m and $Q_c = \sim 2.5$ in water (Fig. 22.2). Their back side is coated with a gold film with a thickness of ~20 nm to gain enough reflectivity of light for the OBD detection of cantilever deflection. Unfortunately, the state-of-the-art cantilevers are not yet placed on the market. Somewhat larger cantilevers, BL-AC10DS-A2 (Olympus: f_c in air 1.5 MHz, f_c in water 600 kHz, and $k_c \sim 0.1$ N/m) or USC-F1.2-k0.15 (NanoWorld: f_c in air 1.2 MHz, f_c in water ~500 kHz, and $k_c \sim 0.15$ N/m), are available in the market. It may be possible to fabricate smaller cantilevers with higher f_c, without increasing k_c larger than 0.1 N/m. However, a smaller cantilever with $w < 1\mu$m could not be of practical use because of difficulty of focusing a laser beam onto such a small cantilever.

As mentioned above, the small cantilevers developed by Olympus are fabricated by thin film deposition of Si_3N_4, not by anisotropic etching of a single silicon crystal. Because of this fabrication method, the cantilevers do not have a sharp tip but a beak-like structure with an apex size of $>20 \times 20\,\text{nm}^2$ as shown in Fig. 22.3 (the size varies chip to tip), which is not sharp enough to obtain high-spatial resolution images. To

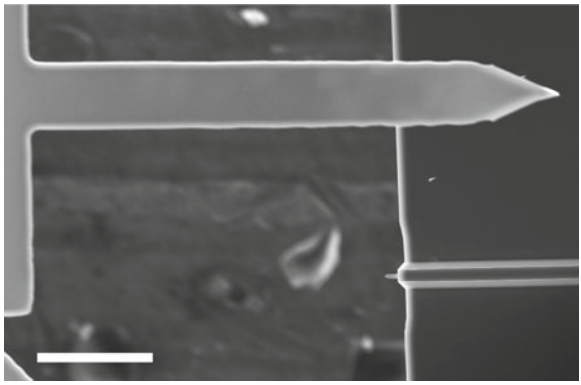

Fig. 22.2 SEM micrograph of a conventional AFM cantilever (*upper*) and a small cantilever (*lower*). Scale bar, 50 μm

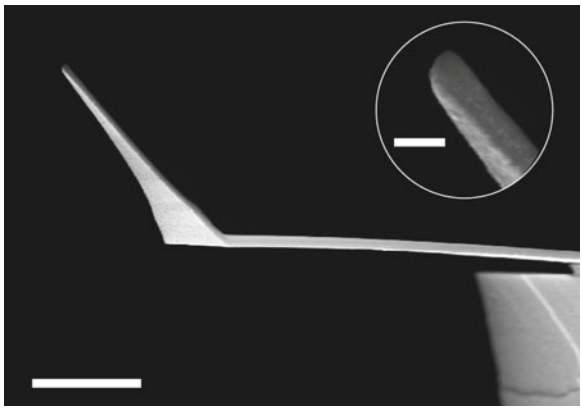

Fig. 22.3 SEM micrograph of a beak-like structure at the free end of an Olympus small cantilever (Scale bar, 1 μm). An *inset* is a magnified view of the end of the beak-like tip (Scale bar, 100 nm)

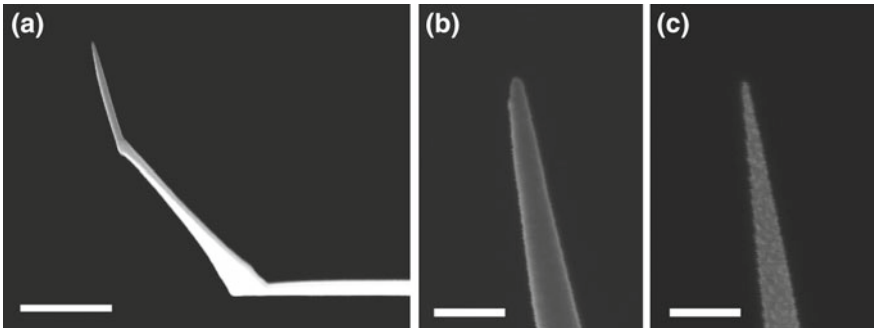

Fig. 22.4 SEM micrographs of EBD tips. **a** Entire view of the EBD tip on the original beak-like tip (Scale bar, 1 μm). The EBD tip ends **b** before and **c** after plasma etching. Scale bars, 100 nm

improve the sharpness, Olympus has grown a sharp carbon nanofiber tip on the beak-like tip. This type of small cantilevers, BL-AC10FS-A2, with mechanical properties similar to those of BL-AC10DS-A2, are also available in the market but expensive. Instead, we grow a sharp tip on the original beak-like tip by irradiating a focused electron beam in the organic gas atmosphere, which is termed the electron-beam deposition (EBD) [34–37]. Sublimable phenol powder is used as an organic gas source in the following way. The powder is placed in a small container with small holes (∼0.1 mm in diameter) in the lid. The cantilevers are attached onto the container lid using a conductive adhesive tape. Then, the container is placed in a scanning electron microscope (SEM) chamber. In the spot mode operation of the SEM, the electron beam of 20 kV is irradiated through an aperture of 20 μm onto the pointed end of the beak-like tip. Under these conditions, a needle composed of amorphous carbon grows at a rate of ∼20 nm/s. The electron beam is usually irradiated for 1 min, resulting in ∼1 μm long EBD tip deposition as shown in Fig. 22.4a. A typical radius of the EBD-tip end is ∼25 nm (Fig. 22.4b). To sharpen it, the cantilever is subjected to plasma etching in argon gas for 3–5 min. This process results in tip-end radius of ∼4 nm (Fig. 22.4c). The mechanical durability of this sharp tip is high enough to capture many images. The EBD tip can be completely removed by plasma etching in oxygen over several hours. Therefore, we can reuse the small cantilever as long as it has no damage and keeps enough light reflexibility.

22.4 OBD System for Small Cantilevers

The OBD method to detect cantilever deflection is simple and easy to use but several cares are required for adapting it to small cantilevers, achieving high sensitive and high bandwidth detection, and minimizing the effect of laser light on biological samples.

Schäffer et al. first reported an OBD system for small cantilevers [38]. A single high numerical aperture (NA) lens was used to have a small focused spot size (7 μm in diameter). The same lens was used to collect and collimate the laser beam reflected back from the cantilever. The collimated reflected laser beam was guided to the photodiode position sensor. However, the short working distance of the single high NA lens restricts the design of the AFM head. Instead of using a single lens, we have been using an objective lens with NA = 0.45 and a long working distance of 8 mm (CFI Plan Fluor ELWD 20×C, Nikon) [15] (Fig. 22.5). The resulting spot size of focused 670 nm laser beam is ∼3 μm in diameter. Because of this strong focusing, the laser power is attenuated to ∼0.5 mW in order to avoid heating the sample. The absence of sample heating was proven by the HS-AFM observation of myosin V molecules moving on actin filaments, where the moving velocity was shown to be identical to those observed by fluorescence microscopy under the same buffer solution and temperature (room temperature) conditions [18]. The same objective lens is also used for the inverted optical microscope integrated with the HS-AFM system to

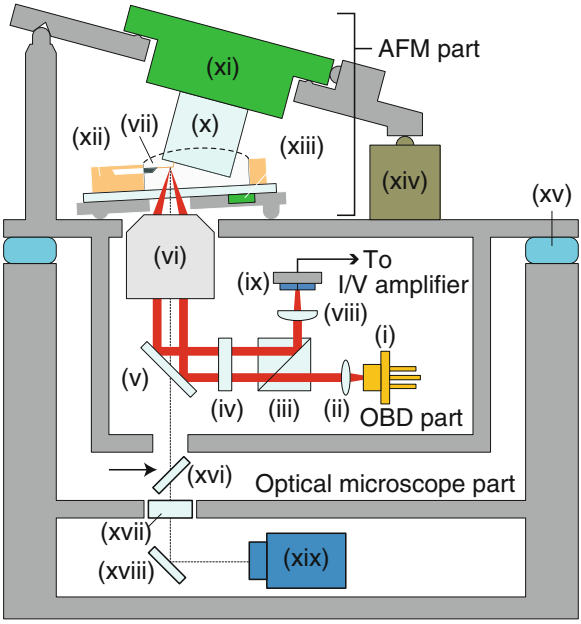

Fig. 22.5 Schematic illustration showing the HS-AFM head integrated with an inverted type of optical microscope. The OBD system comprises *(i)* laser diode, *(ii)* collimator lens, *(iii)* polarization beam splitter, *(iv)* λ/4 plate, *(v)* dichroic mirror, *(vi)* infinity-corrected objective lens, *(viii)* beam shaping lens, and *(ix)* split photodiode. The other devices are *(vii)* cantilever, *(x)* sample stage, *(xi)* high-speed scanner, *(xii)* cantilever holder with liquid cell (*thick dashed line* represents a liquid meniscus), *(xiii)* piezoactuator for cantilever excitation, *(xiv)* stepping motor, *(xv)* soft elastic gels, *(xvi)* dichroic mirror for additional illuminations, *(xvii)* infinity-corrected tube lens, *(xviii)* mirror, *(xix)* digital camera. *Thin dotted line* represents the optical path for the observation of the cantilever and the focused laser spot (See Fig. 22.6)

view the cantilever and the sample stage (more details are given below). To avoid the return of the scattered or reflected laser light into the laser diode, these OBD systems separate the incident and reflected laser beams using a quarter-wavelength plate and a polarization beam splitter (Fig. 22.5).

However, the polarization beam separation method is not perfect. Some of the reflected or scattered laser beam is sometimes incident to the laser diode. When it is incident to the optical resonator of the laser diode, the laser emission becomes unstable and hence noisy due to an "optical feedback" effect [39]. Moreover, some of the scattered light or the laser beam reflected from other objects than the cantilever is sometimes incident to the photodiode position sensor, which optically interferes with the laser beam reflected back from the cantilever and hence produces interference noise. To minimize the return of the reflected laser beam from other objects to the laser diode, one can introduce the incident beam to the objective lens at a slightly off-centered position so that the incident and reflected laser beams pass through different optical paths. Moreover, one can modulate the laser power with an RF signal of 300–500 MHz [39]. By this modulation, the laser oscillation mode is changed from single-mode to multimode. Compared to the single mode, the multimode is much less sensitive to the optical feedback and less coherent and hence less susceptible to optical interference effect. This RF modulation system is implemented in the OBD system of our HS-AFM setup [16].

The reflected light from the cantilever that is collected and collimated by the objective lens is slightly converged and fed into the photodiode position sensor that is a four-segmented Si-PIN photodiode (S6695-01, Hamamatsu Photonics) with a small junction capacitance of 3 pF and a high cutoff frequency of 40 MHz. The photocurrent signal from each segment is converted to voltage and amplified with a fast I/V amplifier and then all the voltage signals are fed into a custom-made signal conditioner with 20 MHz bandwidth to produce an differential output signal proportional to cantilever deflection, as well as a sum signal proportional to the total intensity of laser light incident to the photodiode position sensor. In our typical setup, the OBD detection sensitivity is 50–100 mV/nm, and the deflection noise density is $<$100 fm/$\sqrt{\text{Hz}}$ in water when a laser power of 0.5 mW is used [40].

As mentioned above, our HS-AFM head is combined with a laboratory-made inverted optical microscope that shares the objective lens with the OBD system. This combined system allows easy positioning of the sample stage and the cantilever (Fig. 22.6). The OBD system, to which the objective lens is fixed, is hung from the top base plate of the AFM head (Fig. 22.5). Moreover, the base plate is mechanically uncoupled from the optical microscope using soft elastic gels (e.g., P-N30L, Proseven) (Fig. 22.5). This design effectively shuts out mechanical vibrations that are traveling from the optical microscope with low resonant frequencies.

The optical microscope has an additional optical port (not shown in Fig. 22.5) through which another illumination light can be introduced to the objective lens to irradiate the sample. This light irradiation has been used to image photo-induced structural changes of bacteriorhodopsin [17, 41, 42] and photo-degradations of π-conjugated polymer chains [43]. It has also been used to quickly release functional ligands such as Ca^{2+} and ATP from caged compounds and then observe conforma-

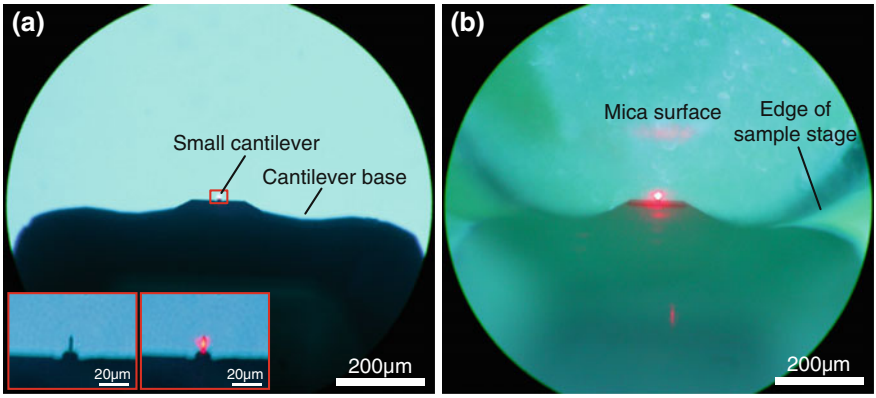

Fig. 22.6 Optical microscopic views of a small cantilever and a sample stage. **a** Low-magnification view of the cantilever without the sample stage. *Insets* show high-magnification views of the *red rectangle region* around the cantilever: *left*, without incident laser; *right*, with incident laser. **b** Low-magnification view of the cantilever when the sample surface is close to the cantilever

tional changes of proteins caused by the interaction with the released ligands [44, 45]. In these applications, the wavelength of the laser diode used in the OBD system sometimes has to be changed from usual 670 nm so that photo-sensitive samples are not affected by the laser beam, as has been done in the above mentioned studies of bacteriorhodopsin, where an infrared laser diode was used in the OBD system.

In addition to the OBD systems described above, other OBD systems or different methods to detect the deflection of small cantilevers have been proposed and used. A method that uses a Fabry-Perot interferometer for in-liquid frequency modulation (FM)-AFM achieved 3 μm focused spot size and a deflection noise density of <3 fm/$\sqrt{\text{Hz}}$ [46, 47]. Fukuma et al. also achieved a similar noise density in-liquid FM-AFM using an OBD system with a highly stabilized laser and a laser driver implemented with an RF signal superposition circuit. This low noise density enabled atomic resolution imaging in liquid [48, 49]. However, note that such a low noise density also requires the use of stiffer cantilevers with small thermal vibration amplitude. The laser diode in an OBD system can be replaced with a superluminescent diode that is low coherent and hence less susceptible to the effects of optical feedback and interference [50].

22.5 Fast Amplitude Detector

Since the Q value of small cantilevers is 2–3 in aqueous solution, the cantilever oscillation amplitude quickly changes when the tip makes contact with the sample surface. Therefore, amplitude detection should be performed at every oscillation cycle. However, RMS-DC converters or lock-in amplifiers used in conventional tapping-mode

AFM setups require at least several oscillation cycles to output an accurate amplitude signal. This is because a low-pass filter is used to remove high harmonic components from the oscillation signal. In the early high-speed AFM setup, a peak-hold method was used, in which the peak and bottom voltages of the oscillation signal were sampled by a sample-and-hold (S/H) circuit and then their difference was output as an amplitude signal [15]. This amplitude detector is fastest that can output the amplitude signal at every half cycle of oscillation. A drawback of this method is that the output is strongly affected by the cantilever's thermal motion because only two data points in the deflection signal are sampled.

In the current high-speed AFM setup, the other type of method, called the Fourier method, is used [16, 51], where the Fourier sine and cosine coefficients (A and B, respectively) of the fundamental frequency component of the deflection signal are calculated and then their root-mean-square, $\sqrt{A^2 + B^2}$, is output as the amplitude. Therefore, the amplitude signal can be detected every oscillation cycle. Since the deflection signal is integrated over a cycle, it provides a less noisy amplitude signal than the peak-hold method. A custom-designed Fourier amplitude detector (Fig. 22.7) composed of analog/digital hybrid circuits has been developed (T3510-01, Tsujicon, Japan), in which a high-performance digital signal processor (DSP) and a field-programmable gate array (FPGA) (StratixIII, Altera Corp., USA) are combined with high-bandwidth analog-to-digital (14 bit, 150 MSPS) and digital-to-analog (14 bit, 12 MSPS) converters. This system can also simultaneously calculate the phase of cantilever oscillation relative to the cantilever's excitation signal, allowing fast phase imaging in tapping mode. Figure 22.8 shows the deflection signal of an oscillating cantilever (red lines) and the amplitude signal (blue lines) detected with the Fourier method. In this measurement, the sinusoidally oscillating cantilever tip was made in

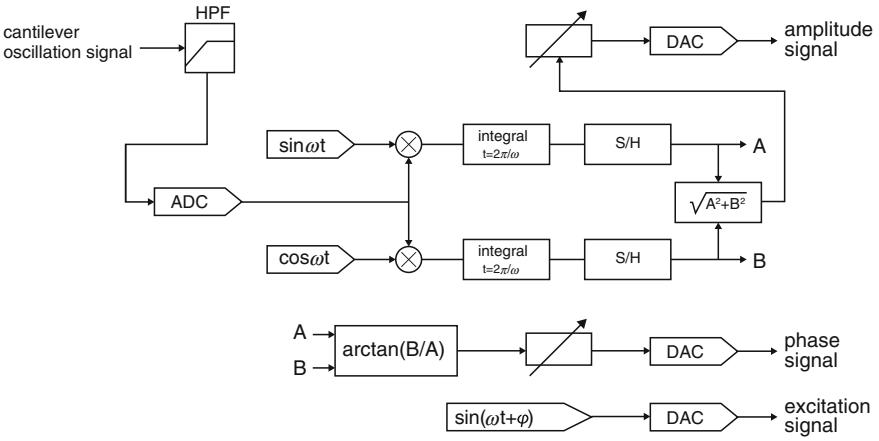

Fig. 22.7 Circuit diagram of Fourier method type of fast amplitude and phase detector

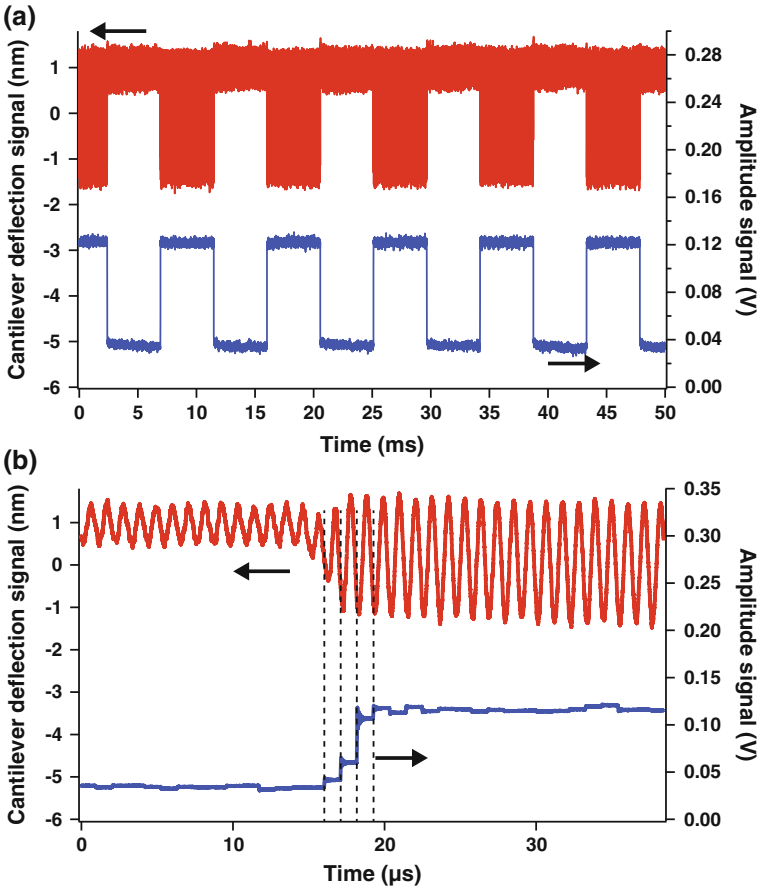

Fig. 22.8 Response of the amplitude detector output to square-wave changes of the cantilever oscillation amplitude. A cantilever is oscillated at 930 kHz in liquid. The Z-scanner was moved up and down by a square wave signal so that the tip was made in contact with the sample periodically. The cantilever's deflection signal and the amplitude signal detected by the Fourier method are plotted by *red* and *blue lines*, respectively. The *broken lines* in (**b**) indicate timings when the output from the amplitude detector is updated

contact periodically with the sample surface that was moved up-and down in a square wave. One can see that the amplitude signal quickly responses to the square-wave changes in the sample Z-position (Fig. 22.8a) and that the output signal is renewed at every oscillation cycle (Fig. 22.8b).

22.6 Scanner

The scanner to be used in high-speed AFM has to meet requirements of both high bandwidth and accuracy in mechanical positioning. The first requirement is most difficult to be achieved because the scanner is composed of macroscopic components such as piezoelectric actuators and supporting mechanical bases. Unwanted mechanical vibrations that limit the operation bandwidth are easily generated by the excitation of flexural vibrations of the mechanical structure. To minimize the generation of unwanted vibrations, piezoactuators with high resonant frequencies and a rigid mechanical structure are needed as well as a novel control strategy to damp unavoidable vibrations. The control for vibration damping is important particularly in the Z-scanner to be driven at high frequencies as well as in wide-area XY-scanners with low resonant frequencies. Moreover, wide-area scanners are susceptible to the effects of inherent nonlinear displacement of piezoactuators and crosstalk between displacements in the X- and Y-axes. Therefore, additional techniques to suppress or compensate for these effects are required. The following sections describe underlying techniques to fulfil these requirements.

22.6.1 Piezoelectric Actuator

Selection of piezoactuators is essential in achieving a high-speed scanner because their resonant frequencies are a major factor that restricts the scan frequency. Among several types of piezo-based actuators, a hollow tube-shaped piezoactuator is one of the simplest designs to achieve three-axis motion and hence has been most commonly used in conventional AFM systems. However, it has a low resonant frequency because of the large length-to-diameter ratio. The first resonant frequency of a tube scanner is typically less than 1 kHz. A shear mode piezoactuator can have a high resonant frequency because of its compact geometry and stiff mechanical property [52]. However, its displacement coefficient (i.e., displacement per voltage) is relatively small, which limits the application range of AFM. Alternatively, a tuning-fork based scanner has been used for video-rate AFM, where the X-scanner is oscillated sinusoidally at the tuning-fork's resonant frequency [53]. However, it has a drawback of non-linear displacement. Although the sinusoidal scan in the X-direction would not excite the scanner's mechanical resonances but makes an AFM image distorted in the X-direction. Generally, stack piezoactuators, which are widely used in commercial flexure-guided nanopositioners, can have both large displacement coefficients and high resonant frequencies. Therefore, stack piezoactuators are probably most suitable for high-speed scanners.

Among the X-, Y-, and Z-scanners, the Z-scanner should have the fastest response without overshoot or oscillation. Its response rate is one of the major factors that determine the bandwidth of feedback control to maintain the tip-sample interaction force constant. We have used different types of stack piezoactuators, depending on

the required displacement ranges. One end of the Z-piezoactuator is usually fixed onto a supporting base that is scanned in the X- and Y-directions. By this holding of the Z-piezoactuator, its resonant frequency becomes half the original one in free oscillation. Furthermore, the mass of the sample stage attached to the other end of the Z-piezoactuator further lowers the resonant frequency. To minimize the mass addition, we use a light glass rod of 1.5–2 mm in diameter and 2 mm long (10–15 mg) as a sample stage. This rod is glued onto the top of the Z-piezoactuator using nail polish.

As to the X-scanner that is scanned in a triangle wave, its resonant frequency should ideally be about 20 times higher than the fundamental frequency of the triangle wave. However, lower resonant frequencies are acceptable because the driving signal is predetermined and therefore feedforward control for vibration damping can be used, as described in Sect. 22.7.2.

22.6.2 Scanner Design

The scanner should be designed to be mechanically rigid so that excitation of unwanted vibrations can be prevented. A flexure-guided mechanism is most suitable for fast scanners because they can be monolithically machined from a single piece of metal block and hence no assembling parts are needed except for piezoactuators. Figure 22.9a illustrates a high-speed scanner that has been used for narrow-area high-speed imaging of biomolecular samples. The whole structure is machined monolithically from a stainless steel (SUS304) block. The thickness of each flexure is 0.4 mm. Two sets of flexure guides are combined in a serial-kinematic configuration; that is, the Y-scanner displaces the XZ-block that is connected to the base frame with two pairs of flexures, while within the XZ-block the X-scanner displaces the Z-scanner that is connected to the frame of the XZ-block with a pair of flexures

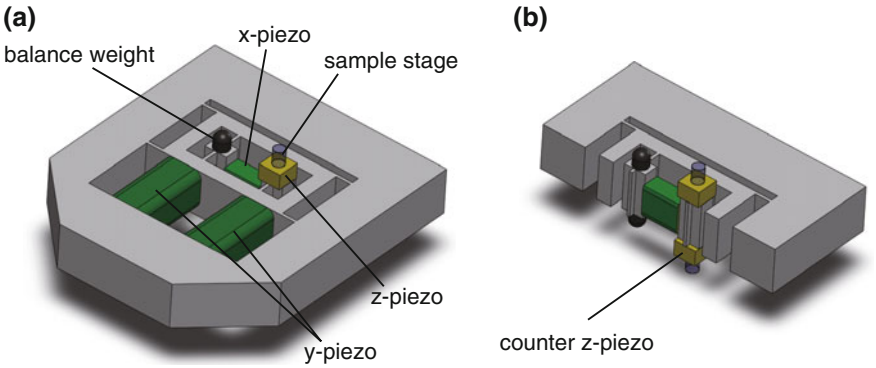

Fig. 22.9 HS-AFM scanner for relatively narrow area scan. The maximum san ranges are 1.3 μm in *X*, 3 μm in *Y* and 1.6 μm in *Z*. **a** Whole and **b** cross-sectional views of the scanner

(see Fig. 22.9a). This serial-kinematic configuration results in an asymmetric structure with respect to the X- and Y-scanners but is adequate because the X-scanner is scanned much faster than the Y-scanner. This configuration has another advantage; it does not suffer from parasitic, off-axis motion and can minimize crosstalk between the three-axis displacements [54]. When a symmetric structure with respect to the X- and Y-scanners is needed, a parallel-kinematic configuration can be employed, as described [55, 56], although this configuration is usually apt to suffer from crosstalk between X- and Y-displacements [54].

Quick displacement of a piezoactuator exerts impulsive force to its supporting base, which causes vibrations of the base and surrounding structures, and in turn, of the piezoactuator itself. To circumvent this problem, the mass center of the X-piezoactuator is managed to be kept stationary by its holding with two identical pairs of flexures at the ends and by the attachment of a balance weight to the counter side (Fig. 22.9a). The mass of the balance weight is adjusted to be similar to the sum of the mass of the Z-piezoactuator and the glass rod sample stage. A similar counterbalancing method is also applied to the Z-scanner. Two identical piezoactuators are attached to the opposite faces of the supporting base as shown in Fig. 22.9b. Both Z-piezoactuators are displaced simultaneously to the same extent in the opposite direction. Thus, the impulsive forces exerted to the supporting base are cancelled with each other [15, 16]. In addition to these devices to suppress unwanted vibrations, the vacant gaps in the scanner are filled with an elastomer to passively damp vibrations. This passive damping is effective in suppressing low-frequency vibrations. In this scanner (Fig. 22.9), stack piezoactuators with dimensions $3 \times 3 \times 2\,\mathrm{mm}^3$ (PL033.30, Physik Instrumente GmbH, Germany; nominal unloaded displacement, 2.2 μm at 100 V; nominal resonant frequency in free oscillation, 600 kHz) are used for the Z-scanner. The resonant frequency and maximum displacement of the Z-scanner with a sample stage are ∼180 kHz and ∼1.6 μm at 100 V, respectively. For the X- and Y-scanners, stack piezoactuators with dimensions $2 \times 3 \times 5\,\mathrm{mm}^3$ (AE0203D04F, Tokin-NEC, Japan; nominal unloaded displacement, 3 μm at 100 V; nominal resonant frequency in free oscillation, 260 kHz) and $5 \times 5 \times 10\,\mathrm{mm}^3$ (AE0505D08F, Tokin-NEC, Japan; nominal unloaded displacement 6 μm at 100 V; nominal resonant frequency in free oscillation, 138 kHz) are used, respectively. The resonant frequencies of these piezoactuators assembled in the scanner are ∼50 kHz and ∼12 kHz, respectively. The maximum displacements of the X- and Y-scanners are ∼1.3 μm and ∼3 μm, respectively.

For wide-area scanning over $\sim 20 \times 20\ \mu\mathrm{m}^2$, there are two ways to achieve such large displacements: one uses long piezoactuators without displacement magnification mechanisms, as has been designed in [55], whereas another uses relatively long piezoactuators together with displacement magnification mechanisms [56]. For wider-area scanning over $> 20 \times 20\ \mu\mathrm{m}^2$, magnification mechanisms are needed because the displacement range of stack piezoactuators with dimensions adequate for HS-AFM systems is limited. Figure 22.10a shows our wide-area scanner with the maximum scan range of $\sim 46 \times 46\ \mu\mathrm{m}^2$ at 100 V [56], where the third-class leverage mechanism is employed to magnify the displacements of the X- and Y-piezoactuators (Fig. 22.10b). This scanner is monolithically machined from an

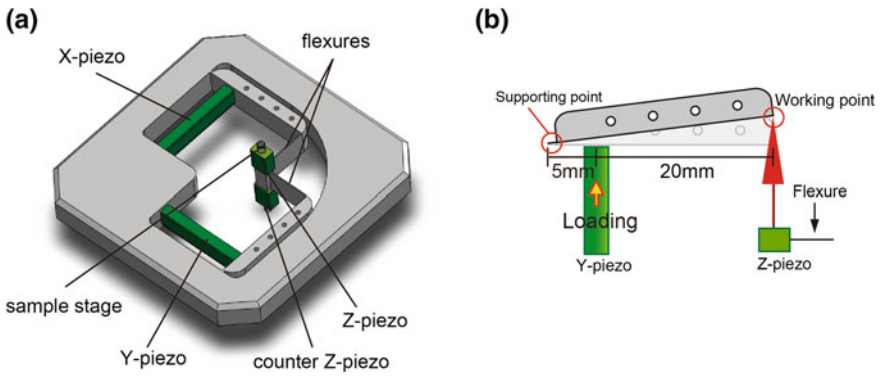

Fig. 22.10 HS-AFM scanner for wide-area scan. The maximum scan ranges are 46 μm in *X* and *Y* and 2.4 μm in *Z*. **a** Whole view of the wide-areas scanner. **b** Leverage-based displacement magnification mechanism

aluminum (A5052) block. The X- and Y-scanners are arranged in a parallel-kinematic configuration. That is, the identical X- and Y-scanners are arranged symmetrically with respect to the supporting base to which the Z-piezoactuator is attached. In this configuration, the fast axis can be chosen arbitrarily for the raster scanning. In the leverage mechanism, the entire lever length is 25 mm and the point of effort to which a piezoactuator is glued is 5 mm distant from the fulcrum; i.e., the designed lever ratio is five. Piezoactuator (AE0203D16F, Tokin-NEC, Japan) used for the X- and Y-scanners have dimensions of $2 \times 3 \times 20\,\text{mm}^3$, a nominal unloaded displacement of 11.6 μm at 100 V and a resonant frequency of 69 kHz. This parallel-kinematic configuration is susceptible to mechanical vibrations and crosstalk between the X- and Y-displacements. Furthermore, nonlinear displacements of the X- and Y-scanners are manifested in a wide-area imaging. These drawbacks have been overcome by feedforward control techniques described in the next sections. A stack piezoactuator (AE0203D04F, Tokin-NEC, Japan) is glued onto the top of the supporting base that is to be moved in the X- and Y-directions. The same type of piezoactuator is also glued to the bottom side of the supporting base as a counterbalance, similar to the small-area scanner.

22.7 Control Techniques

In HS-AFM systems, control techniques are required in various aspects: maintenance of the tip-sample interaction force at its set point, damping of mechanical vibrations of the scanner, compensation for non-linear and coupled displacements in the scanner, and others. In conventional AFM systems, digital controllers are widely used that are based on DSP or FPGA. One of the major advantages of digital controllers is their flexibility. That is, the controllers can be renewed by the update of software or

algorithm without alteration of hardware. Moreover, digital controllers allow us to use sophisticated control schemes that have been proposed to improve the feedback control performance and positioning accuracy in AFM systems [57–64]. However, the time delays involved in digital controllers, such as those required for analog-to-digital (AD) and digital-to-analog (DA) conversions and digital calculations, are not negligible, even when the most advanced digital electronics with highest speed performance are used. We should note that the time delays of mechanical devices of HS-AFM systems (i.e., cantilevers and scanners) have already been shortened significantly. In this current state, the time delay in digital controllers would become a major rate-limiting factor. Considering this advancement, we have been employing an analog proportional-integral-derivative (PID) controller for feedback control of the tip-sample interaction. Moreover, we have developed several control techniques to make high-speed imaging compatible with low-invasive imaging as well as to compensate for non-linear and coupled displacements in the scanner and drift of cantilever excitation efficiency. The following sections describe the details of these control techniques.

22.7.1 Active Damping of Z-scanner Vibrations

The response speed of resonant systems increases with increasing resonant frequency and decreasing quality factor Q. As described in Sect. 22.6, a fast Z-scanner can be built using small stack piezoactuators with high resonance frequencies and the counterbalancing method. However, the Q value of small stack piezoactuators is generally ∼20 or higher (Fig. 22.11a), meaning that there is still room for improving the response speed of the Z-scanner. For cantilevers, an active Q-control technique has been developed to increase their sensitivity to tip-sample interaction by increasing the Q value [65–67]. Conversely, this technique has been used to increase the response speed of cantilevers by decreasing the Q value [68, 69]. In principle, this technique can be applied to any resonant systems.

The Z-scanner motion can be approximately treated as a damped harmonic oscillator driven by external force $F(t)$:

$$m\ddot{z} + \gamma\dot{z} + kz = F(t), \tag{22.6}$$

where m is the mass of the Z-scanner, γ is the damping constant, and k is the spring constant of the Z-scanner, respectively. To decrease the Q value ($= \sqrt{mk}/\gamma$) while keeping the resonant frequency, the damping constant should be increased. To do so, a force proportional to $-\dot{z}$, i.e., $-G\dot{z}$ ($G > 0$), is added to the external force so that the effective Q value (Q_{eff}) decreases to $\sqrt{mk}/(\gamma + G)$. To accomplish this control, the velocity of the Z-scanner should be measured in real time but it is difficult to do so. Instead of measuring the displacement or velocity of the Z-scanner, one can monitor the output signal from a "mock Z-scanner" that is an LRC circuit characterized with a transfer function similar to that of the real Z-scanner [70]. As the transfer function

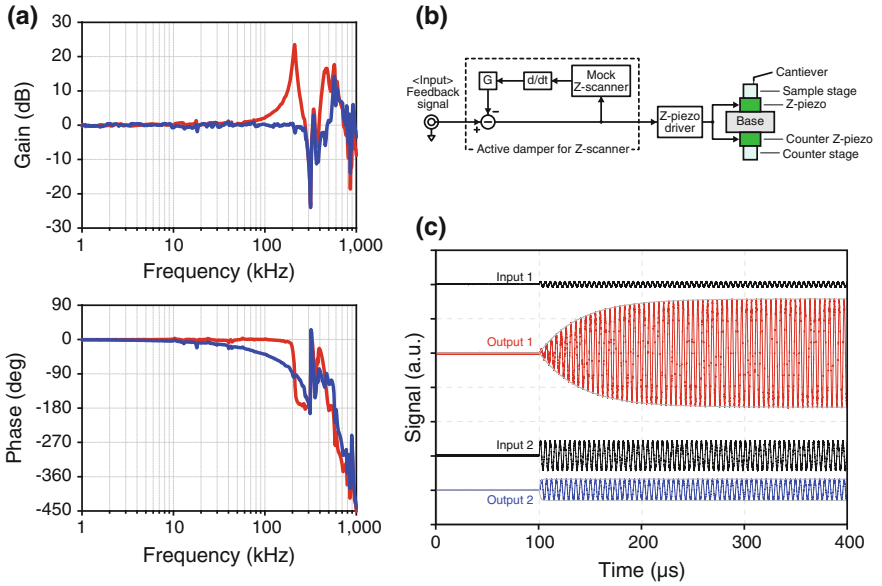

Fig. 22.11 Mock Z-scanner-based method to damp Z-scanner vibrations. **a** Frequency response of the Z-scanner. *Top*, amplitude response; *bottom*, phase response. Without active damping (*red lines*), the first resonant peak appears at 211 kHz, with Q = 28. As the phase of the Z-scanner shows an up-and-down feature around the first and second resonant peaks, the Z-scanner's resonators are connected in parallel. With active damping (*blue lines*), Q_{eff} was set at 0.7. **b** Schematic of the active damping method. The feedback signal (output from the PID controller) is fed to the active damping circuit. The "mock Z-scanner" constructed with an LCR circuit has a very similar frequency response to that of the real Z-scanner. **c** Effect of active damping on the transient response of the Z-scanner. "Input 1" and "Input 2" are the driving signals for the Z-scanner without and with active damping, respectively. The Z-scanner started to be driven at 100 μs by the sinusoidal wave signals of 211 kHz. "Output 1" (*red line*) and "Output 2" (*blue line*) are the responses of the Z-scanner without and with active damping, respectively. *Thin gray lines* represent the envelope curves of the Z-scanner displacements, which indicate the transient changes in the amplitude of the Z-scanner oscillation. The settling times (τ) were 39.0 and 1.0 μs in the cases of without and with active damping, respectively. These values were well consistent with the expectation from the relationship of $\tau = Q/\pi f$, where f was 211 kHz

of the real Z-scanner can be well approximated by that of a second-ordered low-pass filter, the LRC circuit can be easily constructed. This Q-control system is depicted in Fig. 22.11b. This simple method is quite effective in damping Z-scanner vibrations (Fig. 22.11a) and hence in increasing the Z-scanner's response speed (Fig. 22.11c). Although the phase delay is pronounced when Q_{eff} is reduced to 0.5, it can be improved by applying an inverse transfer function compensation, as demonstrated [70]. For practical use, Q_{eff} is set to the critical damping condition (i.e., $Q_{eff} \sim 0.7$). When the resonant frequency of the Z-scanner is high enough so that it would not be excited during imaging, Q_{eff} can be set at 1–3 to avoid pronouncing the phase delay.

22.7.2 Control Techniques to Damp XY-scanner Vibrations

The driving signal for X-directional scan is generally an isosceles triangle wave as a function of time. High harmonic frequency components contained in the vertices of the triangular wave would excite the X-scanner. When the first resonant frequency of the X-scanner is not high enough, this excitation generates fatal vibrations at the X-scanner's resonant frequencies, as exemplified in Fig. 22.12b. To eliminate the generation of unwanted vibrations by raster scanning, non-raster scan patters, such as spiral- [71, 72], cycloid- [73] and Lissajous- [74, 75] patterns, have been proposed. Although these non-raster scan patterns contain no higher harmonic frequencies, the procedures for producing the scan signals, reconstructing the image, and compensating for the nonlinear effects of the piezoactuators are complicated. Moreover, the cantilever tends to be twisted by a lateral dragging force component perpendicular to the lever arm, which would hampers the accurate sample height measurement. Even for wide-area scanners with low resonant frequencies, we still use raster scan but combine two simple methods to suppress the generation of unwanted vibrations in the X-scanner: inversion-based feedforward damping [16, 76, 77] and a modified triangular wave with reduced higher harmonics [16, 78].

The inversion-based feedforward damping is carried out as follows. Supposing that the waveform of X-scan is isosceles triangles characterized by amplitude X_0 and fundamental angular frequency ω_0, its Fourier transform is given by

$$F(\omega) = 2\pi X_0 \left[\frac{1}{2}\delta(\omega) - \frac{2}{\pi^2} \sum_{k=-\infty}^{+\infty} \frac{1}{k^2}\delta(\omega - k\omega_0) \right] \quad (k : odd) \qquad (22.7)$$

To move the X-scanner characterized by a transfer function $G(s)$ in the isosceles triangle waveform, the driving signal X(t) sent to the X-piezoactuator is given by the inverse Fourier transform of constant-gained $F(\omega)/G(i\omega)$, which is expressed as

$$X(t) = g \times \left[\frac{X_0}{2} - \frac{4X_0}{\pi^2} \sum_{k=1}^{+\infty} \frac{1}{k^2} \frac{1}{G(ik\omega_0)} \cos(k\omega_0 t) \right] \quad (k : odd), \qquad (22.8)$$

where g is the constant gain. We calculate (22.8) in advance to obtain numerical values of X(t) and output them in succession from a computer through a D/A converter. The black line in Fig. 22.12c shows the modified triangular wave obtained after filtration of a triangular wave through an inverse transfer function $1/G(i\omega)$ that is constructed using the frequency response of the X-scanner shown in Fig. 22.12a. Here, the filtered triangular wave is constructed with the first 20 terms in the Fourier cosine series of an isosceles triangle function. The vibrations observed in the absence of the feedforward damping are significantly suppressed by this damping method. In principle, this damping method can extend the bandwidth of the X-scanner, but in practice the limited gain and driving current of a piezodriver at high frequencies limit the bandwidth extension. Moreover, the frequency response of the X-scanner varies

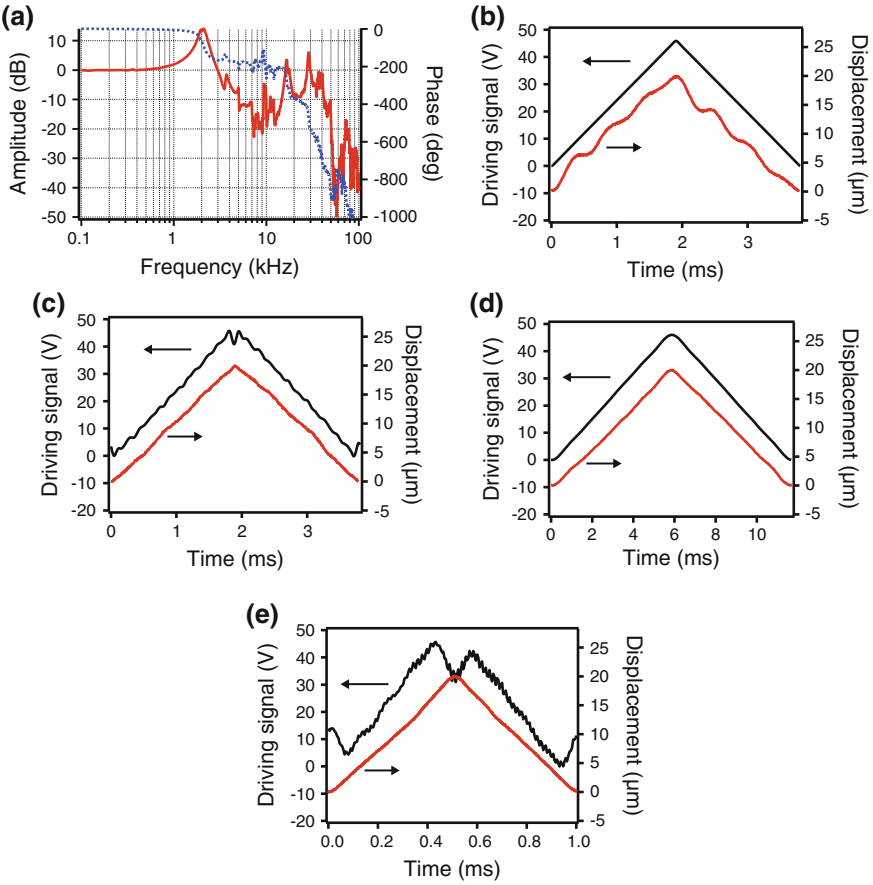

Fig. 22.12 Effects of vibration damping on X-scanner displacement of wide-area scanner. **a** Frequency spectra of mechanical response of the X-scanner (*red line*, amplitude; *blue line*, phase). **b** Driving signal of 256 Hz with a non-modified triangular wave (*black line*) and corresponding displacement (*red line*). **c** Driving signal of 256 Hz with a triangular wave form modified by inverse compensation (*black line*) and corresponding displacement (*red line*). **d** Driving signal of 85 Hz with a rounded triangular wave form containing harmonics up to the ninth order (*black line*) and corresponding displacement (*red line*). **e** Driving signal of 1 kHz obtained after modification by inverse compensation of a rounded triangular wave form containing harmonics up to the ninth-order (*black line*) and corresponding displacement (*red line*)

to some extent depending on the sample attached. Therefore, vibration damping to a practical extent cannot be achieved by this method alone. Therefore, an additional method (simple rounding of the vertices of the triangular wave) is combined.

The simple rounding method is carried out as follows. An isosceles triangular wave is composed of a cosine wave with the fundamental frequency and an infinite series of its odd higher harmonics. By omitting higher harmonic components in this series, we can easily generate a triangular wave with round vertices. As shown in

Fig. 22.12a, the amplitude gain of the X-scanner starts to increase around 500 Hz. Assuming that the gain tolerance is less than 1 dB, the highest frequency of harmonics to be included in the driving signal should be lower than ∼780 Hz, judging from the frequency response shown in Fig. 22.12a. To scan at 85 Hz, the highest harmonics should be less than the ninth order (i.e., 745 Hz). Figure 22.12d shows a rounded triangular wave constructed from harmonics up to the ninth order (black line) and the corresponding displacement of the X-scanner (red line). The displacement does not show noticeable vibrations. The nonlinear scan range is about 10 % of the full scan range, which is much smaller than that when a sinusoidal scan wave is used. Figure 22.12e shows the driving signal and the measured displacement of the X-scanner when the two damping methods are combined. Here, the rounded triangular wave containing higher harmonics up to the ninth order was filtered through an inversed transfer function constructed using the measured frequency response. Thus, the scanning frequency was able to be extended up to ∼1 kHz even for the wide-area scanner with the first resonant frequency of 2 kHz.

In raster scan, a sawtooth wave is usually used for the Y-directional scan. The quick return to the scan origin along the Y-direction, which is performed after the completion of line scans in the X-direction, generates large vibrations. This vibration generation can easily be suppressed by slowing the scan speed. The time delay added by this slow scan is negligible because it is much shorter than the frame imaging time.

22.7.3 Compensation for Nonlinearity and Crosstalk

Piezoelectric materials have hysteresis between driving voltage and displacement. In the X- and Y-directional scan, the positioning error by hysteresis is generally 10–15 % of the full scan range [79], which causes considerable image distortion such as local elongation and compression, especially for wide-area imaging, as demonstrated with a 10 μm-pitch square grid image (Fig. 22.13a). To eliminate image distortion, closed-loop compensation is often used in commercial AFM systems. In the closed-loop compensation, the displacement sensor is incorporated into the scanner to monitor the displacements of the X- and Y-piezoactuators. The monitored displacements are used to regulate the driving signal by feedback control so that the piezoactuators are linearly displaced. This approach enables precise positioning and is tolerant to aging variation of the nonlinearity of the piezoactuators. However, the closed-loop compensation makes the scanner assembly complicated because of the implementation of the displacement sensors. Moreover, the bandwidth of high-precision displacement sensors is too low compared to the bandwidth required for high-speed scanners. On the other hand, open-loop compensation based on pre-measured nonlinear behaviors [80] does not require modification of the scanner and guarantees high-speed performance, although the accuracy would not be as superb as closed-loop compensation.

We applied open-loop compensation to the above wide-area scanner in the following way. The hysteresis curves of the X- and Y-scanners are first measured with a

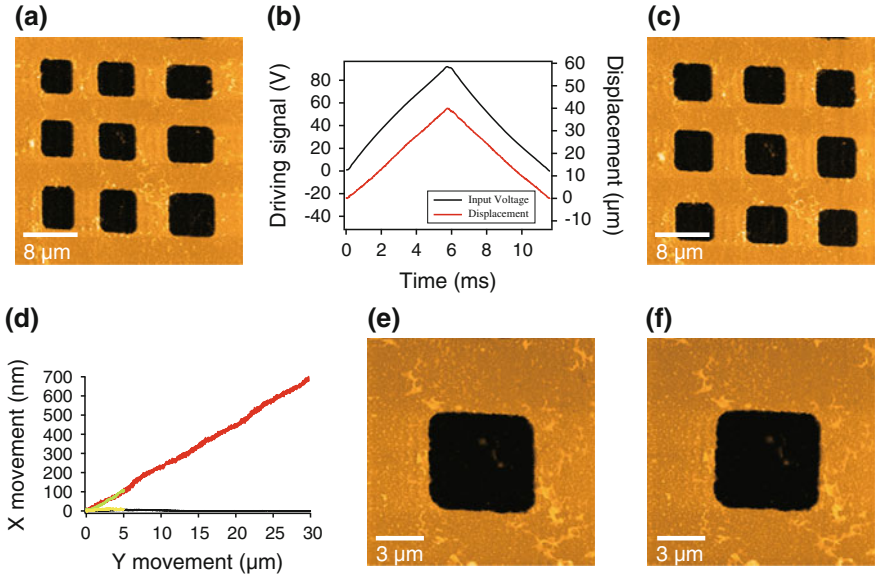

Fig. 22.13 Compensation for nonlinear behavior of piezoactuators and crosstalk between X- and Y-scanning. **a** AFM image of a test grating sample with a pitch of 10 μm obtained without compensation for nonlinear hysteresis (imaging rate, 7 s/frame; pixels, 256 × 256). **b** Driving signal of 85 Hz with a triangular wave form modified by open-loop compensation for hysteresis (*black line*) and corresponding displacement (*red line*). **c** AFM image of the same grating sample obtained with compensation for hysteresis (imaging rate, 7 s/frame; pixels, 256 × 256). **d** Sample stage displacement in the X-direction as a function of Y-scanner displacement. Displacement ranges of Y-scanner are 5 μm (*green line*) and 30 μm (*red line*). *Yellow* and *black lines* represent displacements in the X direction when compensation for crosstalk is applied to Y-scanner displacements of 5 and 30 μm, respectively. **e** AFM image of the grating sample obtained without compensation for crosstalk (scan range, 15 × 15 μm^2, imaging rate, 7 s/frame, pixels, 256 × 256). **f** AFM image of the grating sample obtained with compensation for crosstalk (scan range, 15 × 15 μm^2; imaging rate, 7 s/frame; pixels, 256 × 256)

displacement sensor and then fitted by fourth-order polynomial functions. Although higher-order polynomial functions give better fitting, the fourth-order fitting is good enough in practice to compensate for the nonlinearity. The driving voltage signal not processed for inverse vibration damping is constructed using the inverse functions of the fitted hysteresis curves. Then, this driving signal is further processed by the vibration damping methods mentioned above. Figure 22.13b shows the effect of hysteresis compensation on the displacement of the X-scanner. The black line indicates a driving signal of 85 Hz constructed by open loop compensation, while the red line indicates the corresponding displacement of the X-scanner. The outwardly (ascending regime) and inwardly (descending regime) distorted curves of the driving signal reflect the compensation for the nonlinear hysteresis. The X-scanner is displaced linearly in both expansion and contraction regimes. As a result, the distortion of the grating image is much improved as shown in Fig. 22.13c.

In addition to the nonlinear behavior of the piezoactuators, crosstalk between the X- and Y-scanners is an issue to be resolved for accurate high-speed imaging. Interference between the X- and Y-scanners is inevitable in wide-area scanners that employ the parallel-kinematic configuration. The crosstalk ratio is 0.017 in our wide-area scanner; when the sample stage is moved by 1 μm along one axis, it is also moved by 17 nm along the other axis (Fig. 22.13d). To eliminate the crosstalk effect, an appropriate fraction of the voltage applied to the X (or Y)-piezoactuator is subtracted from the driving signal for the Y (or X)-piezoactuator. This simple method minimizes the coupled movement of the sample stage, irrespective of the displacement range. As a result, the images of square grid holes with rhombic distortion shown in Fig. 22.13e is converted to images with much less distortion, as shown in Fig. 22.13f.

22.7.4 Dynamic PID Controller

Biological phenomena occurring in biomolecules proceed through delicate intramolecular and intermolecular interactions. To observe biomolecular processes using HS-AFM, the tip-sample interaction force should be kept as small as possible. Under the condition of cantilever's free oscillation amplitude A_0 and amplitude set point $A_s = rA_0$, the average tapping force $\langle F_{ts} \rangle$ exerted on the sample from an oscillating cantilever tip is given by

$$\langle F_{ts} \rangle = \frac{k_c A_0}{Q_c} \sqrt{1 - r^2} \tag{22.9}$$

To achieve small $\langle F_{ts} \rangle$ with a given cantilever, the cantilever free oscillation amplitude A_0 has to be set at a small value, and moreover the dimensionless amplitude set point r has to be set close to 1 [81].conditions result in tip parachuting, as described in Sect. 22.2. This problem cannot be solved by the increase of the feedback gain because it induces overshoot in the uphill regions of the sample, resulting in the instability of the feedback operation. However, if the feedback gain can be increased only in the downhill regions of the sample, this difficult problem can be solved.

To accomplish such gain control, we first need to know in real time whether the sample is being scanned in its downhill regions or uphill regions. As described in Sect. 22.2, in the uphill regions the cantilever oscillation amplitude A becomes smaller than the set point amplitude A_s, whereas in the downhill regions A becomes larger than A_s. Using this general rule, we developed a new PID controller called "dynamic PID controller", in which the feedback gain is automatically tuned depending on the relative magnitude of A compared to a threshold level A_H [26]. As shown in Fig. 22.14a, A_H is set at A_s or between A_s and A_0. When A exceeds A_H, an artificial error signal proportional to $(A - A_H)$ is added to the true error signal (Fig. 22.14a, b). The resulting large error signal produces a large feedback signal, which remarkably shortens the parachuting time or prevents the cantilever tip from getting into the parachuting state (Fig. 22.14c). This favorable effect can occur even when r is set up to ~0.9. In fact, the feedback bandwidth becomes independent of r so long as r

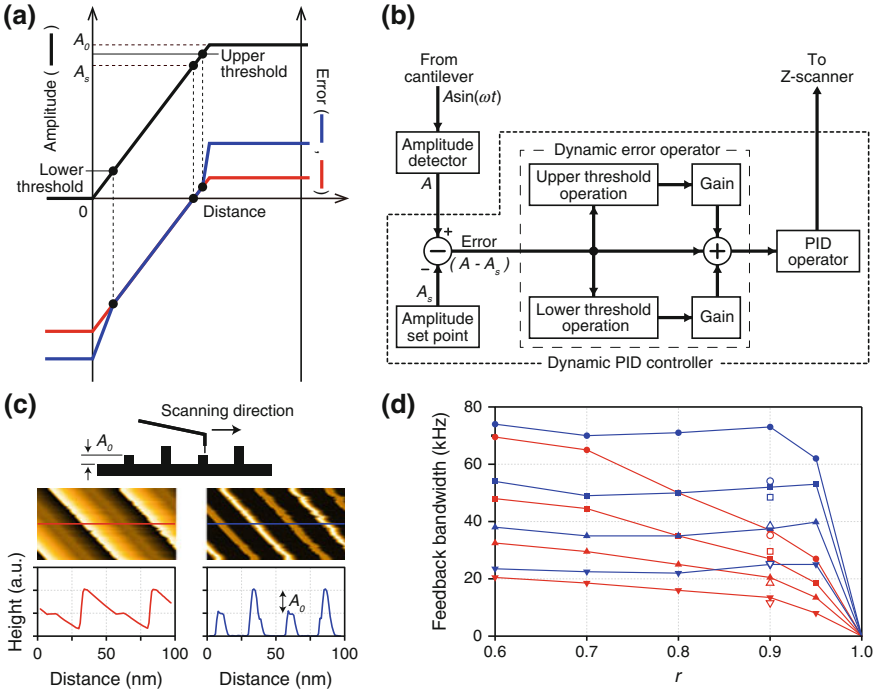

Fig. 22.14 Dynamic PID controller and its effect on feedback bandwidth. **a** Principle of dynamic PID controller. *Black solid line* shows cantilever oscillation amplitude versus distance curve. *Red* and *blue lines* show error versus distance curves for conventional PID control and dynamic PID control, respectively. **b** Circuit diagram of the dynamic PID controller. A dynamic error operator is inserted between the error signal output terminal and the input terminal of the conventional PID operator. Dynamic error signal manipulation is carried out using a precision diode circuit. **c** AFM images of a pseudo-sample surface with rectangle patterns with two different heights. *Top row* shows the schematic of the pseudo-sample surface. *Middle row* shows AFM images taken using the conventional (*left*) and dynamic PID controllers (*right*), respectively. These images were obtained using a mock AFM system [26]. *Bottom row* shows the height profiles along the *red* and *blue lines* drawn in the Pseudo-AFM images. Simulation condition used in the mock AFM system: Cantilever, resonant frequency 1.2 MHz and quality factor 3; Z-scanner, resonant frequency 150 kHz and quality factor 0.5; Sample, height of the lower rectangle A_0 and height of the higher rectangle $2A_0$; the feedback amplitude set point $r = 0.9$; the line scan speed 1 mm/s (1 kHz); Scanning direction from *left* to *right*. **d** Effect of the dynamic PID controller on the feedback bandwidth as a function of the amplitude set point. *Red* and *blue* colored data sets were obtained using the conventional and dynamic PID controllers, respectively. *Filled* and *opened* marks represent the data points obtained by the mock AFM system and the real AFM system (at only $r = 0.9$), respectively. The sample heights for data points of circles, squares, triangles and inverted triangles were $0.2 \times A_0$, $0.5 \times A_0$, $1.0 \times A_0$ and $2.0 \times A_0$, respectively. The other simulation conditions of the mock AFM system were same as that used in (**c**)

is set at less than ∼0.9 (Fig. 22.14d). Thus, this control method makes high-speed imaging compatible with low-invasive imaging to a significant extent. In addition, this gain tuning method can be applied to a situation where the cantilever tip suddenly

encounters an object with significantly large height. In this case, another threshold level A_L is set at a very small value between A_s and zero (Fig. 22.14a, b). When A becomes smaller than A_L, an artificial error signal proportional to $(A - A_L)$ is added to the true error signal. This error signal manipulation can alleviate the event where the cantilever tip gets into a strong contact with the sample.

22.7.5 Drift Compensator

High-speed and low-invasive AFM imaging of biological molecules is typically performed under the condition of $1 < A_0 < 3\,\text{nm}$ and $r = 0.8$–0.9. In order to make the dynamic PID control effective under this condition, both low-noise cantilever oscillation amplitude signal and stable cantilever excitation are required. The former requirement can be satisfied by the Fourier method-based amplitude detector as mentioned in Sect. 22.5. However, the latter requirement is not easy to be met. The cantilever excitation instability is caused by two effects. One is temperature increase in the piezoactuator that is continuously oscillated to excite the cantilever. This temperature increase results in decrease of oscillation efficiency of the piezoactuator. The other is a shape change of the buffer solution in the liquid cell. When A_0 decreases, A also decreases. The feedback control system misinterprets this decrease of A as a consequence of strong tip-sample contact and therefore withdraws the sample stage from the cantilever, which eventually resulting in complete detachment of the tip from the sample surface.

Because there is no direct way to measure A_0 during imaging, it is difficult to maintain A_0 at its initial value. When A_0 is gradually decreasing, A is maintained at its set point by feedback control. However, the tip-sample interaction force is not maintained constant but gradually decreasing. Therefore, it is possible to detect the decrease of A_0 if a signal sensitive to the tip-sample interaction force is available. When a cantilever tip sinusoidally oscillating at f_c taps the sample surface, its sinusoidal oscillation is distorted, resulting in production of higher harmonic components $(2f_c, 3f_c, \ldots)$. The time-averaged amplitude of the second harmonic oscillation can be used as an indicator of drift in A_0 [82]. The second harmonic amplitude can be maintained constant using a slow integral-controller whose time constant is longer than the image acquisition time (Fig. 22.15a). In this way, the amplitude of driving signal for the cantilever-excitation piezoactuator can be controlled to maintain A_0 at its initial value [26]. This drift compensation method works effectively (Fig. 22.15b). Using this method together with the dynamic PID controller, we can perform stable low-invasive and high-speed imaging even under the condition of $A_0 = 1\,\text{nm}$ and $r \sim 0.95$.

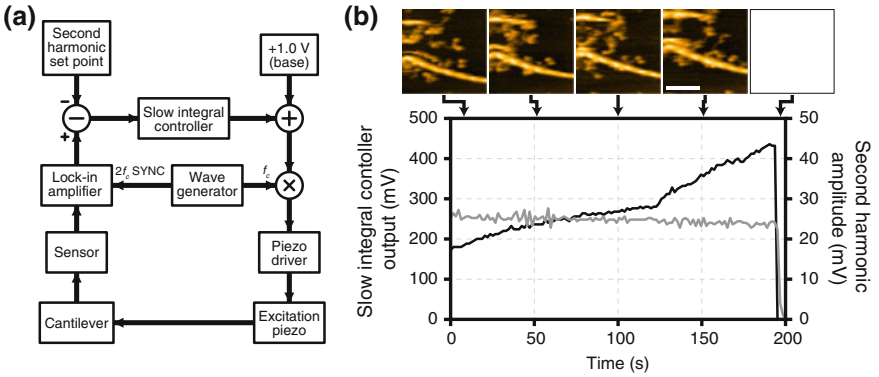

Fig. 22.15 Compensation for drift of cantilever excitation power. **a** Circuit diagram of the drift compensator. The lock-in frequency of the lock-in amplifier is the synchronized second harmonic frequency ($2f_c$) of the cantilever oscillation. **b** Successive AFM images of myosin V molecules bound to actin filaments captured using the drift compensator. The *lower graph* shows the time courses of the output signal from the slow integral controller (*black line*) and the second harmonic amplitude (*gray line*), respectively. The *top row* AFM images were captured at the times indicated by the *arrows*. Imaging conditions: $A_0 = 2.5$ nm; $r = 0.92$; scanning area, 250×250 nm^2; frame rate, 10 fps. At 3 min, the drift compensator was switched off. After that, no image was obtained because of complete detachment of the cantilever tip form the sample surface. Scale bar, 100 nm; Z-scale, 0–11 nm

22.8 HS-AFM Imaging of Protein Molecules in Action

After the completion of development of various devices and techniques described above, HS-AFM was established around 2008. Since then, its innovative power has been continuously demonstrated by the visualization of several types of dynamic events occurring in protein systems (see Reviews [83–85]). These dynamic events include mechanical actions, dynamic interactions with partners, self-assembly processes, diffusion and interactions in membranes, structural transitions, and others. Most of the visualized dynamic events were able to be interpreted straightforwardly without intricate analyses and hypotheses. More importantly, most of the studies brought important discoveries impossible to be made with other approaches, and therefore, provided significant insights into the functional mechanism of the observed protein systems. In this section, HS-AFM imaging studies on myosin V and an intrinsically disordered protein FACT protein are described. For other proteins systems, see [84].

22.8.1 Myosin V

Myosin V (M5) is a member of the myosin superfamily and functions as a cargo transporter in cells. M5 consists of two identical heavy chains, each of which has a

N-terminal motor domain, a neck (also called "lever-arm") domain bound to six light chains (calmodulins or calmolulin-like proteins), a tail region with a proximal α-helix domain to form a dimerized coiled-coil region and a distal C-terminal cargo binding domain [86]. Single molecules of M5 move processively along actin filaments over long distances [87, 88] with a large step size (~36 nm) [87, 89]. This processivity has allowed us to trace the motor action continuously using single-molecule fluorescent microscopy and optical-trap nanometry, enabling the investigation of motor properties of M5. Single molecule studies have demonstrated that M5 moves along actin filaments in a "hand-over-hand" manner [90, 91], consuming one ATP molecule per forward step [92]. However, the protein molecules themselves are invisible in these single molecule observations. Although the structural information has been obtained in detail by electron microscopy [93–96] and X-ray crystallography [97, 98], it has been limited to static snapshots. As such, a comprehensive understanding of the motor mechanism, especially the chemo-mechanical coupling mechanism, has not been achieved until our direct observation of M5 molecules in dynamic action by HS-AFM [18].

To visualize M5 molecules moving along actin filaments with HS-AFM, actin filaments should be immobilized on a surface, while M5 should be free from the surface and interact only with the immobilized actin filaments. To meet these conditions, a mica supported lipid bilayer containing a biotin-lipid was used [99]. On this surface, partially biotinylated actin filaments were immobilized though streptavidin molecules with a low surface density. Successive AFM images captured in the presence of ATP clearly showed individual M5-HMM (tail-truncated myosin V) molecules moving processively with discrete ~36 nm steps (Fig. 22.16a). In the two-headed bound M5-HMM, the neck-motor domain junction appears smooth in the leading head (L-head) but is V-shaped in the trailing head (T-head) without exception. The short coiled-coil tail slightly tilts towards the direction opposite to the moving direction of M5-HMM. These features are fully consistent with those observed by electron microscopy [93]. Furthermore, the detailed stepping process including "hand-over-hand" movement was successfully visualized when the surface density of streptavidin molecules was increased (Fig. 22.16b). The extra amounts of streptavidin molecules worked as moderate obstacles to the stepping. Notably, after the T-head detached from actin, the nearly straight L-head swung from the back leaning orientation to the forward leaning orientation. This observation provided the first direct evidence for the swinging lever-arm motion initially proposed by Huxley for muscle myosin [100]. Thus, the long-lasted debate on this swinging-lever arm hypothesis is now settled and therefore this brilliant idea is no longer a hypothesis [101, 102].

Even under the nucleotide-free condition, both heads of M5-HMM were bound to the same actin filament. However, unlike in the presence of nucleotides, where the T-head almost always (>95 %) took a nearly straight conformation (slightly curved outward), the L-head often exhibited a sharply kinked conformation and alternated back and forth between this conformation and the nearly straight conformation. The sharp kink is likely to occur to release the large strain accumulated in the neck, suggesting that the neck-motor domain junction is stiffer in the absence of nucleotides than that of the nucleotide-bound head. The sharply kinked conformation adopted

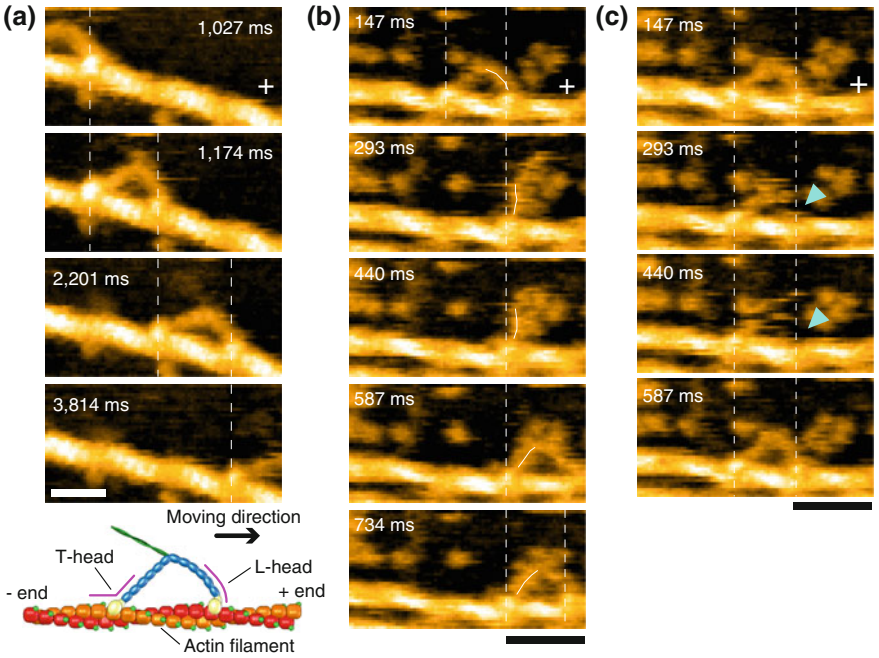

Fig. 22.16 HS-AFM images showing M5-HMM behaviors. **a** Successive AFM images showing unidirectional processive movement of M5-HMM (*upper panels*; scale bar, 30 nm) and schematic showing two-headed bound M5-HMM (*bottom*). **b** Successive AFM images that captured the stepping behavior of M5-HMM (scale bar, 50 nm). The swinging lever-arm is highlighted with the *thin white lines*. **c** Successive AFM images showing a foot stomp event that occurs at the L-head. *Light-blue arrowheads* indicate the detached L-head. The *vertical dashed lines* drawn in the AFM images show the centers of mass of the motor domains, and the *plus signs* indicate the plus ends of actin filaments. These AFM images were taken at 7 fps in a buffer solution containing 1 μM ATP

by the L-head under the nucleotide-free condition can provide a useful indicator of whether or not the L-head contains a nucleotide. Even in the presence of 0.1 μM ATP, the L-head neck was mostly straight (>98 %), suggesting that the L-head almost always retains ADP until the T-head binds to ATP and then detaches from actin. In the presence of low concentrations of ADP, the L-head exhibited alternate switching between the straight and sharply kinked conformations. From the proportion and lifetime of the straight L-head as a function of ADP concentration, the ADP dissociation rate constant k was estimated to be $k = 0.1\,s^{-1}$. The ADP dissociation rate constant of 0.1 s^{-1} means that, on average, one ADP is released from the L-head every 10 s. However, M5-HMM walks many steps during 10 s. As such, the sequential events of ADP release, the subsequent ATP binding, and the resulting head dissociation take place solely at the T-head, which is the basis underlying the processive hand-over-hand walking. This mechanism had been inferred from various indirect experiments [103, 104] but was clearly and directly demonstrated by the HS-AFM observation.

The HS-AFM observations mentioned above provided corroborative visual evidence for previously found or speculated molecular actions of M5. However, HS-AFM observations also brought new discoveries of the chemo-mechanical coupling in M5. During the two-headed bound state, both motor domains frequently exhibited brief dissociation and reassociation on the same actin filament (Fig. 22.16c), whereas M5-HMM remained at approximately the same position on the filament. This behavior was termed "foot stomp". The foot stomp at the L-head raises an important question about the chemo-mechanical coupling in this motor. The briefly detached L-head does not carry bound Pi because Pi is immediately released from the head following the initial attachment of the ADP-Pi-bound head to actin [105]. Nevertheless, the detached ADP-bound L-head rebound to actin still in the back leaning orientation, and then swung its lever-arm forward upon T-head detachment from actin, very similar to the normal step process. This indicated that tension generation for forward movement can occur without transitioning through the ADP-Pi bound state, but directly in the ADP-bound state. Thus, the tension generation for forward movement does not seem to require chemical energy be supplied by ATP hydrolysis. This surprising view was further confirmed by the HS-AFM observation of the two-headed bound M5-HMM in the presence of ADP; the short coiled-coil tail sometimes unwound, after which the monomerized L-head immediately rotated to the forward leaning orientation, very similar to the swinging lever-arm motion occurring in walking M5. This new view on the chemo-mechanical coupling in tension generation and lever-arm swing must be the case not only in M5 but also in all members of the myosin superfamily. This issue of chemo-mechanical coupling and chemical energy usage is described in detail elsewhere [84, 106, 107]. Because this new idea has not been able to be acquired from conventional biophysical and biochemical approaches, this HS-AFM study clearly demonstrates that direct observations of proteins in dynamic action is a powerful new approach to understanding how the proteins function.

22.8.2 Intrinsically Disordered Proteins

Until recently, it has long been believed that all functional proteins adopt a defined three-dimensional ordered structure. In other words, disordered proteins have been believed to be denatured and hence not functional. However, it has recently been recognized that a large fraction of functional proteins do not adopt an ordered structure either entirely or partly. This new class of proteins is referred to as intrinsically disordered proteins (IDPs) [108–111]. Based on a computational genomic analysis, ~30 % of eukaryotic proteins are mostly disordered, and more than 50 % of eukaryotic proteins have intrinsically disordered regions (IDRs) consisting of more than 40 consecutive amino acid residues [112]. In eukaryote, IDPs more frequently exist in nucleus rather than in cytoplasm and often play roles as regulators in transcription, translation and cellular signal transduction [113–115].

Various studies have been performed to understand how IDPs can function and interact with partner molecules [116–118]. In this context, various structural analyses of IDPs have been attempted but it has been difficult to reveal the structure because IDRs are very thin and flexible and transit among many conformers. For example, X-ray crystallography cannot be used because IDRs hamper crystallization. Electron microscopy also cannot be used because IDRs are too thin to be visualized. Therefore, rather indirect methods have often been used and combined to localize and characterize IDRs, such as circular dichroism, proteolysis, small angle X-ray scattering and others. Of course, NMR spectroscopy has been best instrumental in specifying IDRs within an IDP [119–121]. However, NMR spectroscopy can only determine the local structure of IDPs with molecular weights of less than 50 kDa (usually less than 20 kDa). In addition, NMR suffers from the inherent ensemble averaging, and hence, the individual structures populated in the conformational ensemble cannot be determined from NMR data.

As a model IDP, *Drosophila melanogaster* facilitates chromatin transcription (FACT) protein (dFACT) expressed in *E. coli* was used to examine whether HS-AFM would be able to visualize the thin and flexible structure of IDRs [122]. dFACT is a heterodimer consisting of SSRP1 and SPT16 subunits, each of which is predicted to have a long IDR [123–125]. HS-AFM successfully visualized two tail-like structures with different lengths, protruding from the main body of dFACT. Using dFACT mutants, in which either predicted IDRs were deleted, the tail-like structures were verified to be IDRs. It was also confirmed that the longer and shorter IDRs belong to SSRP1 and SPT16, respectively. Note that in the visualization of IDRs the sample cannot be dried because IDRs become too thin to be visualized, meaning that conventional AFM cannot be used for the identification of IDRs because IDRs move fast in solution.

Both two IDRs of dFACT exhibited undulation motion. To characterize the IDRs, the end-to-end distances R of the IDRs were measured, from the averages of which their microscopic persistence lengths L_p were estimated. Interestingly, both IDRs gave a similar value of $L_p \sim 1.1$ nm, in spite of the different amino acid sequences. This value is significantly longer than those of typical ordered proteins, 0.36–0.5 nm [126, 127] and even that of the putative random coil region of titin (i.e., the PEVK region), 0.4–2.5 nm (0.93 nm on average) [128]. Thus, the long L_p is a fingerprint of IDRs [122]. A recent HS-AFM study on other IDPs gave a similar value of L_p [129]. This quantitatively similar property of IDRs can be used to estimate the number of amino acids N_{aa} contained in an IDR, because the following relationship exists:

$$\langle R^2 \rangle = 4L_p \times N_{aa} \times \langle d_{aa} \rangle, \tag{22.10}$$

where $\langle d_{aa} \rangle$ represents the average distance between two adjacent amino acids.

IDRs are frequently subjected to post-translational modifications, including phosphorylation, acetylation, methylation, sumoylation and ubiquitination [130–132]. The IDR of the SSRP1 subunit of dFACT can be phosphorylated. By the phosphorylation, the binding of nucleosomal DNA to dFACT is inhibited [133]. To elucidate this

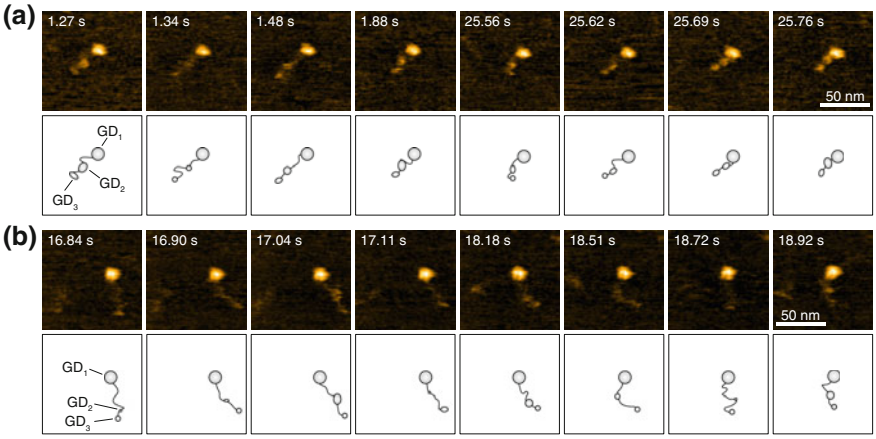

Fig. 22.17 Clips of successive HS-AFM images showing an IDP, dFACT. **a** Phosphorylated form (dFACT-WT) and **b** nonphosphorylated form (dFACT-10SA). The images were taken at 67.08 ms/frame. The time stamp of each image is shown in the *upper left*. Scan area, 100 × 100 mm^2 with 80 × 80 pixels; Z-scale, 4.0 nm. The observed molecular features of dFACT are schematized under the AFM images, which were drawn freehand by tracing the AFM images by visual estimation. *Gray-colored ellipses* and *black thick solid lines* represent the globular domains and IDRs, respectively

inhibitory mechanism, the HS-AFM images of fully phosphorylated form (dFACT-WT) were compared to those of nonphosphorylated form (dFACT-10SA) expressed in Sf9 insect cells [134]. The IDR of SPT16 subunit was deleted from both constructs. As shown in Fig. 22.17, the both constructs exhibited a large globular domain (GD_1), from which a flexible tail-like IDR was protruded, as previously observed [122]. In addition, small globular domains were observed on the middle of the IDR and at the distal end of the IDR. These were termed GD_2 and GD_3, respectively. GD_3 exhibited similar characteristics between the two constructs, whereas GD_2 was temporally appearing and disappearing, with different lifetimes between the two constructs. The GD_2 of dFACT-WT exhibited a longer lifetime in the globular state and larger height than those of dFACT-10SA. Moreover, the mean length of the IDR between GD_1 and GD_2 was shorter by ∼2 nm in dFACT-WT than in dFACT-10SA. Because the position of GD_2 is consistent with the position of the HMG domain that is known to interact with nucleosomal DNA, these observations suggest that the phosphorylated IDR between GD_1 and GD_2 tends to interact with the HMG domain and that this interaction prohibits the HMG domain from interacting with nucleosomal DNA [134]. As has been demonstrated in these studies as well as in other studies on different IDPs (the Archaeal Hef protein consisting of the helicase and nuclease domains [135] and the bacterial flagellar hook-length control protein FliK [136]), HS-AFM is a powerful tool to identify and characterize IDPs [137].

22.9 Future Prospects

Thus far, the innovative power of HS-AFM has been demonstrated in a limited number of proteins. There is, however, no doubt that HS-AFM will be more extensively used in the near future to understand not only the functional mechanism of a diverse array of proteins but also various non-biological dynamic phenomena occurring in liquids at the nanometer scale. To finalize this chapter, we briefly describe the future prospects for further progress of HS-AFM techniques.

The feedback bandwidth of HS-AFM is currently ~100 kHz, which corresponds to the highest possible imaging rate of ~15 fps when protein molecules are targets. This rate limit arises mainly from the limited miniaturization of cantilevers and partly from other devices including the OBD detector. Here we examine whether or not we can increase the feedback bandwidth up to 1 MHz and hence the imaging rate to ~150 fps. To achieve this rate in the tapping mode, the cantilevers made of Si_3N_4 have to have a resonant frequency of ~10 MHz in water whilst the spring constant is kept similar to that of current small cantilevers (~0.2 N/m). Supposing that the damping effect of aqueous solutions on the resonant frequency is similar between the current and expected cantilevers, this resonant frequency in water corresponds to ~35 MHz in air. Under the conditions of $k_c = 0.2$ N/m and width $w = 300$ nm (approximately corresponding to a minimized spot size of focused laser beam), the thickness-to-length ratio d/L is estimated to be ~0.021 from (22.5). From this ratio and (22.4), the resonant frequency in air, f_c, is given by $f_c = 32.3/L$. Therefore, to achieve $f_c = 35$ MHz, L and d should be 0.92 μm and 19 nm, respectively. To focus a laser beam onto such a small cantilever, we have to use an objective lens with a high numerical aperture >0.7 but the incident laser beam with a large incident angle >44° would be interrupted by the supporting base of the cantilever. Considering this interruption effect, the minimum length should be $L \sim 2$ μm, which corresponds to $d \sim 42$ nm and the highest possible $f_c \sim 16$ MHz in air. This frequency is ~4.6 times higher than that of our currently smallest cantilevers. This high resonant frequency may allow us to achieve $R_{max} \sim 70$ fps. To achieve this imaging rate, the X-scanner has to be scanned at ~7 kHz, while the Z-scanner has to be scanned at ~460 kHz. These numbers appear to be still within a feasible range, considering the scan ranges required for imaging protein molecules (~100 nm for the XY-directions and ~50 nm for the Z-direction) and available piezoactuators. To go beyond $R_{max} = 70$ fps, we have to discard the tapping mode and instead use the torsional mode [138] because the resonant frequency of torsional cantilever vibrations is much higher than that of flexural vibrations. Then, the factors that limit R_{max} would be piezoactuators and the mass of the sample stage.

In the HS-AFM system described above, the sample stage is scanned in three directions, while the cantilever chip is stationary. This type of system simplifies the AFM head structure because the focused spot position of the laser beam for OBD detection can be stationary. However, this configuration does not allow us to use a large sample stage. Moreover, it does not allow us to combine HS-AFM with fluorescence microscopy or various optical techniques, thus limiting the expandability

of HS-AFM. Recently, we developed the tip-scan type of HS-AFM system, in which the focused laser beam of the OBD detector precisely tracks the XY-motion of the cantilever [139]. This tracking is carried out by tilting, around orthogonal two axes, a dichroic mirror that reflects the laser beam. By placing this tip-scan HS-AFM system on an inverted type of fluorescence microscope, HS-AFM and total internal reflection fluorescence microscopy (TIRFM) images can be simultaneously captured, as demonstrated [139]. This combined tip-scan mode HS-AFM allows us to introduce various optical techniques. For example, optical tweezers can be installed in the combined system. This system will allow us to visualize a single biological molecule under external force. This visualization will provide a new opportunity to study the effect of applied force on the action of the molecule as well as detailed unfolding and refolding processes of the molecule. It is also possible to introduce tip-enhanced fluorescence microscopy that is based on the highly enhanced electric field formed in the close vicinity of a laser-illuminated metal or silicon tip [140, 141]. Tip-enhanced fluorescence microscopy has resolution <10 nm [142]. Therefore, this installation will materialize super-resolution/high-speed fluorescence microscopy combined with HS-AFM. As such, further progress will be expected to extend both speed performance and functionality of HS-AFM.

References

1. F.J. Giessibl, S. Hembacher, H. Bielefeldt, J. Mannhart, Science **289**, 422 (2000)
2. Y. Sugimoto, P. Pou, M. Abe, P. Jelinek, R. Perez, S. Morita, O. Custance, Nature **446**, 64 (2007)
3. D. Rugar, R. Budakian, H.J. Mamin, B.W. Chui, Nature **430**, 329 (2004)
4. F.J. Giessibl, Appl. Phys. Lett. **73**, 3956 (1998)
5. B. Cappela, G. Dietler, Surf. Sci. Rep. **34**, 1 (1999)
6. J.P. Cleveland, B. Anczykowski, A.E. Schmid, V.B. Elings, Appl. Phys. Lett. **72**, 2613 (1998)
7. R.A. Oliver, Rep. Prog. Phys. **71**, 076501 (2008)
8. U. Hartmann, Annu. Rev. Mater. Sci. **29**, 53 (1999)
9. B. Gotsmann, M.A. Lantz, Nat. Mater. **12**, 59 (2012)
10. U. Rabe, W. Arnold, Appl. Phys. Lett. **64**, 1493 (1994)
11. O. Kolosov, K. Yamanaka, Jpn. J. Appl. Phys. **32**, L1095 (1993)
12. L. Zhang, Y. Ju, A. Hosoi, A. Fujimoto, Rev. Sci. Instrum. **81**, 123708 (2010)
13. M. Jaschke, H.-J. Butt, Langmuir **11**, 1061 (1995)
14. R.D. Piner, J. Zhu, F. Xu, S. Hong, C.A. Mirkin, Science **283**, 661 (1999)
15. T. Ando, N. Kodera, E. Takai, D. Maruyama, K. Saito, A. Toda, Proc. Natl. Acad. Sci. U.S.A. **98**, 12468 (2001)
16. T. Ando, T. Uchihashi, T. Fukuma, Prog. Surf. Sci. **83**, 337 (2008)
17. M. Shibata, H. Yamashita, T. Uchihashi, H. Kandori, T. Ando, Nat. Nanotechnol. **5**, 208 (2010)
18. N. Kodera, D. Yamamoto, R. Ishikawa, T. Ando, Nature **468**, 72 (2010)
19. T. Uchihashi, R. Iino, T. Ando, H. Noji, Science **333**, 755 (2011)
20. K. Igarashi, T. Uchihashi, A. Koivula, M. Wada, S. Kimura, T. Okamoto, M. Penttila, T. Ando, M. Samejima, Science **333**, 1279 (2011)
21. R.C. Barrett, C.F. Quate, J. Vac. Sci. Technol. B **9**, 302 (1991)
22. S.C. Minne, J.D. Adames, G. Yaralioglu, S.R. Manalis, A. Atalar, C.F. Quate, Appl. Phys. Lett. **73**, 1742 (1998)

23. T. Ando, T. Uchihashi, N. Kodera, D. Yamamoto, A. Miyagi, M. Taniguchi, H. Yamashita, Pflügers Archiv-Eur. J. Physiol. **456**, 211 (2008)
24. T. Itani, J.J. Santillan, Appl. Phys. Express **3**, 061601 (2010)
25. T. Uchihashi, N. Kodera, T. Ando, Nat. Protoc. **7**, 1193 (2012)
26. N. Kodera, M. Sakashita, T. Ando, Rev. Sci. Instrum. **77**, 083704 (2006)
27. D. Sarid, *Scanning Force Microscopy: With Applications to Electric, Magnetic, and Atomic Forces* (Oxford University Press, New York, 1994)
28. G.E. Fantner, G. Schitter, J.H. Kindt, T. Ivanov, K. Ivanova, R. Patel, N. Holten-Andersen, J. Adams, P.J. Thurner, I.W. Rangelow, P.K. Hansma, Ultramicroscopy **106**, 881 (2006)
29. J.A. Harley, T.W. Kenny, Appl. Phys. Lett. **75**, 289 (1999)
30. S. Hosaka, K. Etoh, A. Kikukawa, H. Koyanagi, J. Vac. Sci. Technol. B **18**, 94 (2000)
31. M. Kitazawa, K. Shiotani, A. Toda, Jpn. J. Appl. Phys. **42**, 4844 (2003)
32. M.B. Viani, T.E. Schaffer, A. Chand, M. Rief, H.E. Gaub, P.K. Hansma, J. Appl. Phys. **86**, 2258 (1999)
33. D.A. Walters, J.P. Cleveland, N.H. Thomson, P.K. Hansma, M.A. Wendman, G. Gurley, V. Elings, Rev. Sci. Instrum. **67**, 3583 (1996)
34. T. Fujii, M. Suzuki, M. Miyashita, M. Yamaguchi, T. Onuki, H. Nakamura, T. Matsubara, H. Yamada, K. Nakayama, J. Vac. Sci. Technol. B **9**, 666 (1991)
35. B. Hubner, H.W.P. Koops, H. Pagnia, N. Sotnik, J. Urban, M. Weber, Ultramicroscopy **42**, 1519 (1992)
36. H.Y. Ximen, P.E. Russell, Ultramicroscopy **42**, 1526 (1992)
37. J.H. Kindt, G.E. Fantner, J.B. Thompson, P.K. Hansma, Nanotechnology **15**, 1131 (2004)
38. T.E. Schäffer, J.P. Cleveland, F. Ohnesorge, D.A. Walters, P.K. Hansma, J. Appl. Phys. **80**, 3622 (1996)
39. T. Fukuma, M. Kimura, K. Kobayashi, K. Matsushige, H. Yamada, Rev. Sci. Instrum. **76**, 126110 (2005)
40. T. Uchihashi, N. Kodera, T. Ando, in *Atomic Force Microscopy in Nanobiology*, ed. by K. Takeyasu. Development of High-Speed AFM and Its Biological Applications (Pan Stanford Publishing, Singapore, 2014), p. 143
41. M. Shibata, T. Uchihashi, H. Yamashita, H. Kandori, T. Ando, Angew. Chem. Int. Ed. Engl. **50**, 4410 (2011)
42. H. Yamashita, K. Inoue, M. Shibata, T. Uchihashi, J. Sasaki, H. Kandori, T. Ando, J. Struct. Biol. **184**, 2 (2013)
43. K. Shinohara, N. Kodera, T. Oohashi, J. Polym. Sci., Part A: Polym. Chem. **48**, 4103 (2010)
44. T. Ando, N. Kodera, Y. Naito, T. Kinoshita, K. Furuta, Y.Y. Toyoshima, Chem. Phys. Chem. **4**, 1196 (2003)
45. T. Ando, N. Kodera, T. Uchihashi, A. Miyagi, R. Nakakita, H. Yamashita, K. Matada, J. Surf. Sci. Nanotechnol. **3**, 384 (2005)
46. B.W. Hoogenboom, P.L.T.M. Frederix, J.L. Yang, S. Martin, Y. Pellmont, M. Steinacher, S. Zach, E. Langenbach, H.J. Heimbeck, Appl. Phys. Lett. **86**, 074101 (2005)
47. B.W. Hoogenboom, H.J. Hug, Y. Pellmont, S. Martin, P.L.T.M. Frederix, D. Fotiadis, A. Engel, Appl. Phys. Lett. **88**, 193109 (2006)
48. T. Fukuma, K. Onishi, N. Kobayashi, A. Matsuki, H. Asakawa, Nanotechnology **23**, 135706 (2012)
49. H. Asakawa, Y. Katagiri, T. Fukuma, Jpn. J. Appl. Phys. **52**, 110109 (2013)
50. A. Colom, I. Casuso, F. Rico, S. Scheuring, Nat. Commun. **4**, 2155 (2013)
51. J. Kokavecz, Z. Toth, Z.L. Horvath, P. Heszler, A. Mechler, Nanotechnology **17**, S173 (2006)
52. M.J. Rost, L. Crama, P. Schakel, E. van Tol, G.B.E.M. van Velzen-Williams, C.F. Overgauw, H. ter Horst, H. Dekker, B. Okhuijsen, M. Seynen, A. Vijftigschild, P. Han, A.J. Katan, K. Schoots, R. Schumm, W. van Loo, T.H. Oosterkamp, J.W.M. Frenken, Rev. Sci. Instrum. **76**, 053710 (2005)
53. L.M. Picco, L. Bozec, A. Ulcinas, D.J. Engledew, M. Antognozzi, M.A. Horton, M.J. Miles, Nanotechnology **18**, 044030 (2007)
54. Y.K. Yong, S.O.R. Moheimani, B.J. Kenton, K.K. Leang, Rev. Sci. Instrum. **83**, 121101 (2012)

55. C. Braunsmann, T.E. Schäffer, Nanotechnology **21**, 225705 (2010)
56. H. Watanabe, T. Uchihashi, T. Kobashi, M. Shibata, J. Nishiyama, R. Yasuda, T. Ando, Rev. Sci. Instrum. **84**, 053702 (2013)
57. G. Schitter, F. Allgower, A. Stemmer, Nanotechnology **15**, 108 (2004)
58. G. Schitter, P. Menold, H.F. Knapp, F. Allgower, A. Stemmer, Rev. Sci. Instrum. **72**, 3320 (2001)
59. Q. Zou, K.K. Leang, E. Sadoun, M.J. Reed, S. Devasia, Asian J. Control **6**, 164 (2004)
60. A. Stemmer, G. Schitter, J.M. Rieber, F. Allgower, Eur. J. Control **11**, 384 (2005)
61. Y. Wu, Q.Z. Zou, IEEE Trans. Control Syst. Technol. **15**, 936 (2007)
62. S. Necipoglu, S.A. Cebeci, Y.E. Has, L. Guvenc, C. Basdogan, IEEE Trans. Nanotechnol. **10**, 1074 (2011)
63. J. Otero, H. Guerrero, L. Gonzalez, M. Puig-Vidal, Sensors **12**, 686 (2012)
64. M.W. Fairbairn, S.O.R. Moheimani, IEEE Control Syst. **33**, 46 (2013)
65. B. Anczykowski, J.P. Cleveland, D. Kruger, V. Elings, H. Fuchs, Appl. Phys. A: Mater. Sci. Process. **66**, S885 (1998)
66. J. Tamayo, A.D.L. Humphris, A.M. Malloy, M.J. Miles, Ultramicroscopy **86**, 167 (2001)
67. J. Tamayo, A.D.L. Humphris, R.J. Owen, M.J. Miles, Biophys. J. **81**, 526 (2001)
68. T. Sulchek, R. Hsieh, J.D. Adams, G.G. Yaralioglu, S.C. Minne, C.F. Quate, J.P. Cleveland, A. Atalar, D.M. Adderton, Appl. Phys. Lett. **76**, 1473 (2000)
69. M. Antognozzi, M.D. Szczelkun, A.D.L. Humphris, M.J. Miles, Appl. Phys. Lett. **82**, 2761 (2003)
70. N. Kodera, H. Yamashita, T. Ando, Rev. Sci. Instrum. **76**, 053708 (2005)
71. I.A. Mahmood, S.O.R. Moheimani, B. Bhikkaji, IEEE Trans. Nanotechnol. **10**, 203 (2011)
72. T.R. Meyer, D. Ziegler, C. Brune, A. Chen, R. Farnham, N. Huynh, J.M. Chang, A.L. Bertozzi, P.D. Ashby, Ultramicroscopy **137**, 48 (2014)
73. Y.K. Yong, S.O.R. Moheimani, I.R. Petersen, Nanotechnology **21**, 365503 (2010)
74. A. Bazaei, Y.K. Yong, S.O.R. Moheimani, Rev. Sci. Instrum. **83**, 063701 (2012)
75. T. Tuma, J. Lygeros, V. Kartik, A. Sebastian, A. Pantazi, Nanotechnology **23**, 185501 (2012)
76. Y. Li, J. Bechhoefer, Rev. Sci. Instrum. **78**, 013702 (2007)
77. G. Schitter, A. Stemmer, IEEE Trans. Control Syst. Technol. **12**, 449–454 (2004)
78. K.K. Leang, A.J. Fleming, Asian J. Control **11**, 144 (2009)
79. P. Ge, M. Jouaneh, IEEE Trans. Control Syst. Technol. **4**, 209 (1996)
80. B. Mokaberi, A.A.G. Requicha, IEEE Trans. Autom. Sci. Eng. **5**, 197 (2008)
81. T.R. Rodriguez, R. Garcia, Appl. Phys. Lett. **82**, 4821 (2003)
82. J. Schiener, S. Witt, M. Stark, R. Guckenberger, Rev. Sci. Instrum. **75**, 2564 (2004)
83. T. Ando, Nanotechnology **23**, 062001 (2012)
84. T. Ando, T. Uchihashi, S. Scheuring, Chem. Rev. **114**, 3120 (2014)
85. T. Ando, T. Uchihashi, N. Kodera, Annu. Rev. Biophys. **42**, 393 (2013)
86. R.E. Cheney, M.K. O'Shea, J.E. Heuser, M.V. Coelho, J.S. Wolenski, E.M. Espreafico, P. Forscher, R.E. Larson, M.S. Mooseker, Cell **75**, 13 (1993)
87. A.D. Mehta, R.S. Rock, M. Rief, J.A. Spudich, M.S. Mooseker, R.E. Cheney, Nature **400**, 590 (1999)
88. T. Sakamoto, I. Amitani, E. Yokota, T. Ando, Biochem. Biophys. Res. Commun. **272**, 586 (2000)
89. M. Rief, R.S. Rock, A.D. Mehta, M.S. Mooseker, R.E. Cheney, J.A. Spudich, Proc. Natl. Acad. Sci. U.S.A. **97**, 9482 (2000)
90. J.N. Forkey, M.E. Quinlan, M.A. Shaw, J.E. Corrie, Y.E. Goldman, Nature **422**, 399 (2003)
91. A. Yildiz, J.N. Forkey, S.A. McKinney, T. Ha, Y.E. Goldman, P.R. Selvin, Science **300**, 2061 (2003)
92. T. Sakamoto, M.R. Webb, E. Forgacs, H.D. White, J.R. Sellers, Nature **455**, 128 (2008)
93. M.L. Walker, S.A. Burgess, J.R. Sellers, F. Wang, J.A. Hammer 3rd, J. Trinick, P.J. Knight, Nature **405**, 804 (2000)
94. S. Burgess, M. Walker, F. Wang, J.R. Sellers, H.D. White, P.J. Knight, J. Trinick, J. Cell. Biol. **159**, 983 (2002)

95. N. Volkmann, H. Liu, L. Hazelwood, E.B. Krementsova, S. Lowey, K.M. Trybus, D. Hanein, Mol. Cell **19**, 595 (2005)
96. O.A. Oke, S.A. Burgess, E. Forgacs, P.J. Knight, T. Sakamoto, J.R. Sellers, H. White, J. Trinick, Proc. Natl. Acad. Sci. U.S.A. **107**, 2509 (2010)
97. P.D. Coureux, A.L. Wells, J. Menetrey, C.M. Yengo, C.A. Morris, H.L. Sweeney, A. Houdusse, Nature **425**, 419 (2003)
98. P.D. Coureux, H.L. Sweeney, A. Houdusse, EMBO J. **23**, 4527 (2004)
99. D. Yamamoto, T. Uchihashi, N. Kodera, H. Yamashita, S. Nishikori, T. Ogura, M. Shibata, T. Ando, Methods Enzymol. **475**, 541 (2010)
100. H.E. Huxley, Science **164**, 1356 (1969)
101. J.A. Spudich, Nat. Rev. Mol. Cell Biol. **2**, 387 (2001)
102. M.A. Geeves, Nature **415**, 129 (2002)
103. C. Veigel, S. Schmitz, F. Wang, J.R. Sellers, Nat. Cell Biol. **7**, 861 (2005)
104. T.J. Purcell, H.L. Sweeney, J.A. Spudich, Proc. Natl. Acad. Sci. U.S.A. **102**, 13873 (2005)
105. E.M. De La Cruz, A.L. Wells, S.S. Rosenfeld, E.M. Ostap, H.L. Sweeney, Proc. Natl. Acad. Sci. U.S.A. **96**, 13726 (1999)
106. T. Ando, FEBS Lett. **587**, 997 (2013)
107. N. Kodera, T. Ando, Biophys. Rev. **6**, 237 (2014)
108. H.J. Dyson, P.E. Wright, Annu. Rev. Phys. Chem. **47**, 369 (1996)
109. A.K. Dunker, C.J. Brown, J.D. Lawson, L.M. Iakoucheva, Z. Obradovic, Biochemistry **41**, 6573 (2002)
110. V.N. Uversky, Protein Sci. **11**, 739 (2002)
111. P. Tompa, *Structure and Function of Intrinsically Disordered Proteins* (Chapman and Hall/CRC, New York, 2009)
112. C.J. Oldfield, Y. Cheng, M.S. Cortese, C.J. Brown, V.N. Uversky, A.K. Dunker, Biochemistry **44**, 1989 (2005)
113. M. Fuxreiter, A. Toth-Petroczy, D.A. Kraut, A.T. Matouschek, R.Y. Lim, B. Xue, L. Kurgan, V.N. Uversky, Chem. Rev. **114**, 6806 (2014)
114. U. Jakob, R. Kriwacki, V.N. Uversky, Chem. Rev. **114**, 6779 (2014)
115. V.N. Uversky, V. Dave, L.M. Iakoucheva, P. Malaney, S.J. Metallo, R.R. Pathak, A.C. Joerger, Chem. Rev. **114**, 6844 (2014)
116. V.N. Uversky, S. Longhi, in *Instrumental Analysis of Intrinsically Disordered Proteins: Assessing Structure and Conformation*, ed. by V.N. Uversky. Protein and Peptide Science (Wiley, New Jersey, 2010)
117. V.N. Uversky, A. Dunker, in *Intrinsically Disordered Protein Analysis*, vol. 1, ed. by V.N. Uversky, A. Dunker. Methods in Molecular Biology, vol. 895 (Humana Press, New York, 2012)
118. V.N. Uversky, A. Dunker, in *Intrinsically Disordered Protein Analysis*, vol. 2, ed. by V.N. Uversky, A. Dunker. Methods in Molecular Biology, vol. 896 (Humana Press, New York, 2012)
119. H.J. Dyson, P.E. Wright, Chem. Rev. **104**, 3607 (2004)
120. M.R. Jensen, R.W. Ruigrok, M. Blackledge, Curr. Opin. Struct. Biol. **23**, 426 (2013)
121. M.R. Jensen, M. Zweckstetter, J.R. Huang, M. Blackledge, Chem. Rev. **114**, 6632 (2014)
122. A. Miyagi, Y. Tsunaka, T. Uchihashi, K. Mayanagi, S. Hirose, K. Morikawa, T. Ando, Chem. Phys. Chem. **9**, 1859 (2008)
123. R. Belotserkovskaya, S. Oh, V.A. Bondarenko, G. Orphanides, V.M. Studitsky, D. Reinberg, Science **301**, 1090 (2003)
124. T. Shimojima, M. Okada, T. Nakayama, H. Ueda, K. Okawa, A. Iwamatsu, H. Handa, S. Hirose, Genes. Dev. **17**, 1605 (2003)
125. T. Formosa, Biochim. Biophys. Acta. **1819**, 247 (2013)
126. D.J. Müller, W. Baumeister, A. Engel, Proc. Natl. Acad. Sci. U.S.A. **96**, 13170 (1999)
127. H. Dietz, M. Rief, Proc. Natl. Acad. Sci. U.S.A. **101**, 16192 (2004)
128. H. Li, A.F. Oberhauser, S.D. Redick, M. Carrion-Vazquez, H.P. Erickson, J.M. Fernandez, Proc. Natl. Acad. Sci. U.S.A. **98**, 10682 (2001)

129. S. Dora, N. Kodera, J. Habchi, D. Blocquel, A. Gruet, T. Mori, M. Lotti, M. Mizuguchi, S. Longhi, T. Ando (Submitted)
130. L.M. Iakoucheva, P. Radivojac, C.J. Brown, T.R. O'Connor, J.G. Sikes, Z. Obradovic, A.K. Dunker, Nucl. Acid. Res. **32**, 1037 (2004)
131. M. Fuxreiter, Mol. Biosyst. **8**, 168 (2012)
132. D. Vuzman, Y. Levy, Mol. Biosyst. **8**, 47 (2012)
133. Y. Tsunaka, J. Toga, H. Yamaguchi, S. Tate, S. Hirose, K. Morikawa, J. Biol. Chem. **284**, 24610 (2009)
134. M. Hashimoto, N. Kodera, Y. Tsunaka, M. Oda, M. Tanimoto, T. Ando, K. Morikawa, S. Tate, Biophys. J. **104**, 2222 (2013)
135. S. Ishino, T. Yamagami, M. Kitamura, N. Kodera, T. Mori, S. Sugiyama, T. Ando, N. Goda, T. Tenno, H. Hiroaki, Y. Ishino, J. Biol. Chem. **289**, 21627 (2014)
136. N. Kodera, K. Uchida, T. Ando, S. Aizawa, J. Mol. Biol. **427**, 406 (2015)
137. T. Ando, N. Kodera, Methods Mol. Biol. **896**, 57 (2012)
138. O. Sahin, S. Magonov, C. Su, C.F. Quate, O. Solgaad, Nat. Nanotechnol. **2**, 507 (2007)
139. S. Fukuda, T. Uchihashi, R. Iino, Y. Okazaki, M. Yoshida, K. Igarashi, T. Ando, Rev. Sci. Instrum. **84**, 073706 (2013)
140. O.F.J. Martin, C. Girard, Appl. Phys. Lett. **70**, 705 (1997)
141. L. Novotny, R.X. Bian, X.S. Xie, Phys. Rev. Lett. **79**, 645 (1997)
142. Z. Ma, J.M. Gerton, L.A. Wade, S.R. Quake, Phys. Rev. Lett. **97**, 260801 (2006)

Index

S. Morita et al. (eds.), *Noncontact Atomic Force Microscopy*,
NanoScience and Technology, DOI 10.1007/978-3-319-15588-3

S